

1 **Highly resolved mapping of NO₂ vertical column densities from** 2 **GeoTASO measurements over a megacity and industrial area during** 3 **the KORUS-AQ campaign**

4 Gyo-Hwang Choo¹, Kyunghwa Lee¹, Hyunkee Hong^{1*}, Ukkyo Jeong^{2,3}, Wonei Choi⁴, Scott J. Janz³

5 ¹Environmental Satellite Center, National Institute of Environmental Research, Hwangyeong-ro 42, Seo-gu, Incheon, Republic
6 of Korea, 22689

7 ²Earth System Science Interdisciplinary Center, University of Maryland, College Park, Maryland, USA 20740

8 ³NASA Goddard Space Flight Center, Greenbelt, Maryland, USA, 20771

9 ⁴Division of Earth Environmental System Science, Major of Spatial Information Engineering, Pukyong National University,
10 Busan 48513, South Korea

11 *Correspondence to:* Hyunkee Hong; Tel: +82 32 560 8437; Fax: +82 32 560 8460; E-mail address: wanju77@korea.kr

12 **Abstract.** The Korea-United States Air Quality (KORUS-AQ) campaign is a joint study between the United States National
13 Aeronautics and Space Administration (NASA) and the South Korea National Institute of Environmental Research (NIER) to
14 monitor megacity and transboundary air pollution around the Korean Peninsula using airborne and ground-based
15 measurements. Here, tropospheric nitrogen dioxide (NO₂) slant column density (SCD) measurements were retrieved from
16 Geostationary Trace and Aerosol Sensor Optimization (GeoTASO) L1B data during the KORUS-AQ campaign (May 2 to
17 June 10, 2016). The retrieved SCDs were converted to tropospheric vertical column densities using the air mass factor (AMF)
18 obtained from a radiative transfer calculation with trace gas profiles and aerosol property inputs simulated with the Community
19 Multiscale Air Quality (CMAQ) model and surface reflectance data obtained from the Moderate Resolution Imaging
20 Spectroradiometer (MODIS). For the first time, we examine highly resolved (250 m × 250 m resolution) tropospheric NO₂
21 over the Seoul and Busan metropolitan regions, and the industrial regions of Anmyeon. We reveal that the maximum NO₂
22 VCDs were 4.94×10^{16} and 1.46×10^{17} molecules cm⁻² at 9 AM and 3 PM over Seoul, respectively, 6.86×10^{16} and $4.89 \times$
23 10^{16} molecules cm⁻² in the morning and afternoon over Busan, respectively, and 1.64×10^{16} molecules cm⁻² over Anmyeon.
24 The VCDs retrieved from the GeoTASO airborne instrument were **some** correlated with those obtained from the Ozone
25 Monitoring Instrument (OMI) (**$r = 0.48$**), NASA's Pandora Spectrometer System (**$r = 0.91$**), and NO₂ mixing ratios obtained
26 from in situ measurements (**$r = 0.07$ in the morning, $r = 0.26$ in the afternoon over the Seoul, and $r > 0.56$ over Busan**). Based
27 on our results, GeoTASO is useful for identifying hotspots of NO₂ and its spatial distribution in highly populated cities and
28 industrial areas.

29 **1 Introduction**

30 Nitrogen dioxide (NO₂) is one of the most important atmospheric trace gases and plays a key role in aerosol production and
31 tropospheric ozone photochemistry (Boersma et al., 2004; Richter et al., 2005). Furthermore, high NO₂ concentrations in the
32 atmosphere have adverse effects on human health, such as respiratory infections, domestic heating, and associated symptoms
33 (Brauer et al., 2002; Latza et al., 2009).

34 The major sources of NO₂ in the atmosphere are from fossil fuel combustion from vehicles and thermal power plants, lightning,
35 flash production, and biogenic soil processes. In addition, it has been found that NO₂ concentrations are highly correlated with
36 population size (Lamsal et al., 2013). The implementation of emission control technology and environmental regulation has
37 led to a decrease in surface NO₂ concentrations in Western Europe, the United States, and Japan in the last few decades (Richter
38 et al., 2005). The NO₂ concentration over major metropolitan cities in South Korea and China are over 3 times larger than over
39 similarly sized cities in Europe and United States, despite NO₂ concentration decreasing in China and South Korea (de Foy et
40 al., 2016, Choo et al., 2020).

41 To date, several low-orbit space borne sensors, such as the Global Ozone Monitoring Experiment (GOME) (Burrows et al.,
42 1999), the Scanning Imaging Spectrometer for Atmospheric Cartography (SCIAMACHY) (Burrows et al., 1995), the Ozone
43 Monitoring Instrument (OMI) (Levelt et al., 2006), the GOME-2 (Callies et al., 2000), and the Tropospheric Monitoring
44 Instrument (TROPOMI) (Veefkind et al., 2012), have monitored atmospheric ozone and its precursors including NO₂ and
45 formaldehyde (HCHO) as a proxy for volatile organic compounds (VOCs). Furthermore, the Geostationary Environment
46 Monitoring Spectrometer (GEMS) (Choi et al., 2018; Kim et al., 2020), which was launched on February 18, 2020, will form
47 a constellation of geostationary satellites including the upcoming Tropospheric Emission: Monitoring of Pollution (TEMPO)
48 (Zoogman et al., 2017) and Sentinel-4 platforms, to continuously observe the air quality of the Northern Hemisphere during
49 the daytime.

50 NO₂ retrievals from space borne hyperspectral measurements are typically conducted using the differential optical absorption
51 spectroscopy (DOAS) method (Platt and Stutz, 2008) to first retrieve the view-dependent slant column density (SCD), and
52 then radiative transfer models are used to determine the vertical column density (VCD) using an air mass factor (AMF)
53 correction. Previous and ongoing space borne instruments use various radiative transfer codes and model input assumptions to
54 calculate NO₂ AMF values at fairly coarse spatial resolution. Because the AMF weighting has a large impact on NO₂ retrievals
55 using the DOAS method, it is important to use model input assumptions that most accurately match the viewing and
56 atmospheric conditions. Several studies have demonstrated the sensitivity of AMF calculations to inaccurate model input
57 parameters (e.g., *a priori* NO₂ vertical profile and aerosol properties) and *a priori* data (cloud information and surface
58 reflectance) (Leitão et al., 2010; Hong et al., 2017; Lorente et al., 2017; Boersma et al., 2018). NO₂ retrievals have also been
59 consistently conducted based on surface remote sensing measurements including the Multi-Axis DOAS (MAX-DOAS),
60 Système D'Analyse par Observations Zénithales (SAOZ) spectrometer (Pastel et al., 2014), and Pandora (Herman et al., 2009)
61 systems. These ground-based measurements can be used as validation references for both airborne and space borne
62 measurements.

63 Furthermore, NO₂ retrievals from airborne remote sensing instruments, such as the Geostationary Coast and Air Pollution
64 Event (GEO-CAPE) Airborne Simulator (GCAS) (Kowalewski and Janz, 2014), the Heidelberg Airborne Imaging DOAS
65 Instrument (HAIDI) (General et al., 2014), the Geostationary Trace gas and Aerosol Sensor Optimization (GeoTASO) (Leitch
66 et al., 2014), the Airborne Prism Experiment (APEX; Popp et al., 2012), the Airborne Imaging DOAS instrument for
67 Measurements of Atmospheric Pollution (AirMAP; Meier et al., 2017; Schönhardt et al., 2015), the Small Whiskbroom Imager
68 for atmospheric composition monitorinG (SWING; Merlaud et al. 2018), and the Spectrolite Breadboard Instrument (SBI;
69 Vlemmix et al., 2017; Tack et al., 2019) have also been performed to identify local emission sources and obtain highly resolved
70 horizontal NO₂ distributions.

71 Observations using airborne measurements have an advantage as they enable the observation of horizontal distributions of
72 trace gases at resolutions higher than space-based satellites and provide data over a wider area than ground-based observations.
73 For example, Nowlan et al. (2018) retrieved tropospheric NO₂ VCDs over Houston, Texas, during the Deriving Information
74 on Surface Conditions from Column and Vertically Resolved Observations Relevant to Air Quality (DISCOVER-AQ)
75 campaign and identified a high correlation with data retrieved from Pandora. Popp et al. (2012) also presented the morning
76 and afternoon NO₂ spatial distribution in Zurich, Switzerland, using APEX. Tack et al. (2017) have conducted high-resolution
77 mapping of NO₂ over three Belgium cities (Antwerp, Brussels, and Liège) using APEX and Judd et al. (2020) and Tack et al.
78 (2021) compared NO₂ VCDs retrieved from GCAS/GeoTASO and APEX with those obtained from TROPOMI over New
79 York City and Antwerp and Brussels, respectively. Merlaud et al. (2013) observed NO₂ VCDs in Turceni over Romania using
80 SWING mounted on an unmanned aerial vehicle (UAV) during the Airborne Romanian Measurements of Aerosols and Trace
81 gases (AROMAT) campaign. These existing NO₂ retrievals, using airborne measurements, have been useful for constraining
82 regional air quality models due to the highly resolved source identification and the ability to tie these results to the ground-
83 based observations.

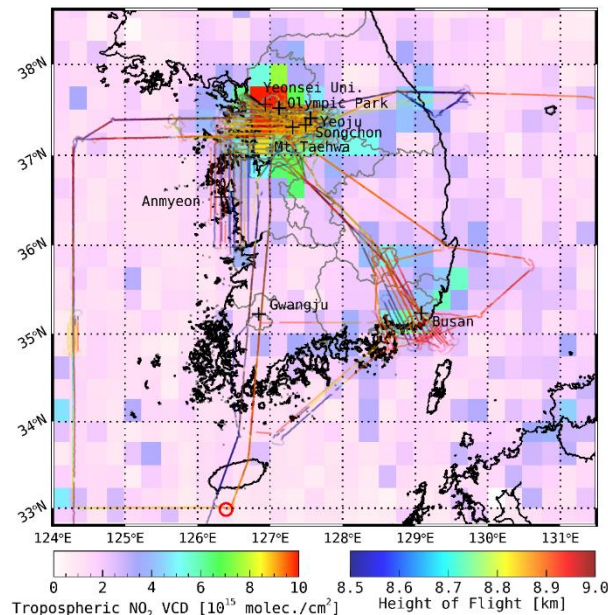
84 This work focuses on airborne NO₂ retrievals from GeoTASO. This instrument was developed by Ball Aerospace to reduce
 85 mission risk for the UV-VIS air quality measurements from geostationary orbit for the GEMS and TEMPO missions (Leitch
 86 et al., 2014). The retrieval of NO₂, SO₂, and HCHO observed from GeoTASO L1B data using DOAS and principal component
 87 analysis (PCA) (Wold et al., 1987) was conducted through the DISCOVER-AQ and KORea-United States Air Quality
 88 (KORUS-AQ) campaigns (Nowlan et al., 2016; Judd et al., 2018; Choi et al., 2020; Chong et al., 2020). The KORUS-AQ
 89 campaign is a joint study between the National Institute of Environmental Research (NIER) and National Aeronautics and
 90 Space Administration (NASA) to monitor megacity air pollution and transboundary pollution, and to prepare for geostationary
 91 satellite (i.e., GEMS, TEMPO, and Sentinel-4) air quality observability (of trace gases and aerosols), organized from May to
 92 June 2016.

93 Although surface NO₂ concentrations in South Korea are high due to high population density, high traffic volumes, and many
 94 industrial complexes and thermal power plants, and whereas NO₂ retrieval studies using airborne and ground measurements
 95 over North America, Europe, China, and Japan have been conducted, data for South Korea remain limited. The specific aims
 96 of this study are as follows:

- 97 (1) To retrieve tropospheric NO₂ vertical column data using GeoTASO measurements over polluted regions of the Seoul
 98 and Busan metropolitan areas and the Anmyeon industrial regions of the Korean Peninsula.
- 99 (2) To estimate NO₂ VCD uncertainties using error propagation accounting for spectral fitting errors and AMF
 100 uncertainties associated with input data errors, including aerosol optical depth (AOD), single scattering albedo (SSA),
 101 aerosol loading height (ALH), and surface reflectance.
- 102 (3) To compare NO₂ VCDs retrieved from GeoTASO and those obtained from OMI and ground-based Pandora
 103 instruments, as well as surface in situ measurements.

104 2 KORUS-AQ campaign area, measurements, and model simulation

105 2.1 Campaign area



106
 107 **Figure 1. Flight paths of the NASA LaRC B200 aircraft carrying GeoTASO and the average tropospheric NO₂ VCDs**
 108 **obtained from OMI gridded to a 0.25°×0.25° horizontal grid during the KORUS-AQ campaign period. The line colour**
 109 **represents flight height. In this period, the GeoTASO observations focused on megacities (Seoul and Busan) and**
 110 **industrial complex area (Anmyeon) with high tropospheric NO₂ concentrations. The reference spectrum for spectral**
 111 **fitting is obtained from the radiation data under the Jeju Island (marked with red circle).**
 112

113 The Korean Peninsula, located on the Asia-Pacific coast, has a complex atmospheric environment by local emissions and long-
 114 range transport under appropriate weather conditions (Jeong et al., 2017; NIER and NASA, 2020; Choo et al., 2021). In
 115 particular, Seoul, the capital of South Korea, and the metropolitan area are densely populated, and power plants and industrial
 116 activities on the northwest coast are carried out, which emits relatively large amounts of pollutants. The KORUS-AQ campaign
 117 conducted three-dimensional observations, including ground-based remote, aircraft, satellite observation, and air quality
 118 modelling, to understand the complex air quality and interpret the observations of GEMS launched in 2020. The KORUS-AQ
 119 campaign period was from May 2 to June 10, 2016. During the KORUS-AQ campaign, measurements of air pollutants were
 120 carried out by using the GeoTASO on board the NASA Langley Research Center B200 aircraft to monitor air quality and long-
 121 range transport of pollutants over the Korean Peninsula (NIER and NASA, 2020). The GeoTASO observations conducted a
 122 total of 30 times over 23 days out of 40 days. Most observations were made once or twice a day. Each flight were planned and
 123 conducted on a day when weather conditions were fine and flight hours were approximately 2-4 hours. We show the average
 124 values of GeoTASO flight information for the dates retrieved for NO₂ VCD, aerosols properties (AOD, SSA) extracted from
 125 CMAQ, and cloud fraction and surface reflectance extracted from the Moderate Resolution Imaging Spectroradiometer
 126 (MODIS) in Table 1. Flight information on the date of aircraft observation can be found in detail at [http://www-](http://www-air.larc.nasa.gov/missions/korus-aq/docs/KORUS-AQ_Flight_Summaries_ID122.pdf)
 127 [air.larc.nasa.gov/missions/korus-aq/docs/KORUS-AQ_Flight_Summaries_ID122.pdf](http://www-air.larc.nasa.gov/missions/korus-aq/docs/KORUS-AQ_Flight_Summaries_ID122.pdf). Figure 1 shows the flight routes of
 128 B200 and the tropospheric NO₂ VCDs obtained from the OMI during the campaign period. The observations were concentrated
 129 in the metropolitan areas of Seoul and Busan and the industrial areas of Anmyeon, with an averaged flight altitude of ~8.5 km
 130 during KORUS-AQ.

131

132 **Table 1. Summary of information on the dates when NO₂ VCD was retrieved during the KORUS-AQ period (LT=UTC+9**
 133 **hr).**

Date	5 Jun	9 Jun AM	9 Jun PM	10 Jun AM	10 Jun PM
ROI	Anmyeon	Seoul metropolitan		Busan metropolitan	
Flight time (LT)	13:11–17:20	7:48–12:00	13:46–17:52	8:02–11:38	13:05–15:19
Flight altitude (km)	8.6	8.4	8.5	8.6	8.5
Flight speed (ms ⁻¹)	117.0	116.2	117.6	117.2	117.1
SZA (°)	39.2	36.1	45.3	35.9	33.0
VZA (°)	168.1	167.4	117.6	117.2	117.1
AOD	0.27	0.40	0.21	0.13	0.09
SSA	0.966	0.980	0.949	0.981	0.968

Surface reflectance	0.07	0.09	0.09	0.06	0.06
Cloud fraction	0.08	0.31	0.55	0.16	0.20

134

135 As shown in Fig. 1, GeoTASO observations were conducted focusing on highly NO₂-polluted regions in the Seoul and Busan
136 metropolitan areas and the Anmyeon region during the KORUS-AQ campaign. The Seoul metropolitan area (Seoul Special
137 City, Gyeonggi Province, and Incheon City) is one of the most densely populated areas worldwide, with a population of
138 approximately 20 million in 2016. Busan is the second-largest city in South Korea, with a population of approximately 3.4
139 million in 2016. Anmyeon is located southwest of Seoul with petrochemical complexes, steel mill works, and thermal power
140 stations in this area. The background colour in Fig. 1 represents the average NO₂ VCD obtained from the OMI during the
141 KORUS-AQ campaign period, showing over 1×10^{16} molecules cm⁻² over the Seoul metropolitan area. The OMI data obtained
142 by the Level 2.0 OMNO2 version 3.0 and downloaded from the NASA's Earthdata search
143 (<http://search.earthdata.nasa.gov/search/>). We calculated the arithmetic means of the tropospheric NO₂ VCDs, similar to Choo
144 et al. (2020), to obtain the grid data (0.25° × 0.25°) during KORUS-AQ period. The average tropospheric NO₂ VCD data were
145 excluded from 30 May 2016 to 9 Jun 2016, when the OMI data did not exist during the campaign period.

146 2.2 Pandora

147 NO₂ VCDs retrieved from the GeoTASO were validated using those from NASA's Pandora Spectrometer system. The Pandora
148 spectrometer is a hyper-spectrometer that can provide direct sun measurements of UV/Vis spectra (280–525 nm with a full
149 width at half maximum (FWHM) of 0.6 nm) for observing atmospheric trace gases. During the KORUS-AQ, eight Pandora
150 instruments monitored NO₂ and ozone (O₃) VCD as depicted by plus symbols in Fig. 1. The retrieved data are available on the
151 KORUS-AQ pages of NASA's Goddard Space Flight Center website
152 (<https://avdc.gsfc.nasa.gov/pub/DSCOVER/Pandora/DATA/KORUS-AQ/>). We compared NO₂ VCDs obtained from five
153 Pandora measurement (Busan university: 35.24 °N, 129.08 °E; Olympic park: 37.52 °N, 127.13 °E; Songchon: 37.41 °N,
154 127.56 °E; Yeosu: 37.34 °N, 127.49 °E; Yonsei University: 37.56 °N, 126.93 °E) within 0.05 degree and 30 min with those
155 from GeoTASO. Because NO₂ has a short atmospheric lifetime, especially during the summer (Shah et al., 2020), its spatial
156 and temporal distributions vary notably. A detailed description of Pandora's operation during the KORUS-AQ campaign has
157 been previously reported (Herman et al., 2018; Spinei et al., 2018).

158 2.3 Ground-based in situ NO₂ measurement

159 Although the basic physical quantity of VCD and surface mixing ratio from in-situ measurements are different, comparison of
160 their spatiotemporal variations provides useful information for deriving surface air quality from airborne instruments (e.g.,
161 Jeong and Hong, 2021a; 2021b). In this study, we compare the NO₂ VCDs (molecules cm⁻²) retrieved from GeoTASO to
162 surface mixing ratios measured by ground-based in-situ monitoring network over South Korea (i.e., Air-Korea, a national real-
163 time air quality network; <https://www.airkorea.or.kr/>). The instruments utilize the chemiluminescence method (Kley and
164 McFarland, 1980), and approximately 400 air quality monitoring sites in Korea are registered in the system, providing hourly
165 surface NO₂ concentrations. We compared NO₂ VCDs retrieved from GeoTASO within 0.5 km and 30 min with NO₂
166 concentrations obtained from Air-Korea.

167 **2.4 GeoTASO measurements**

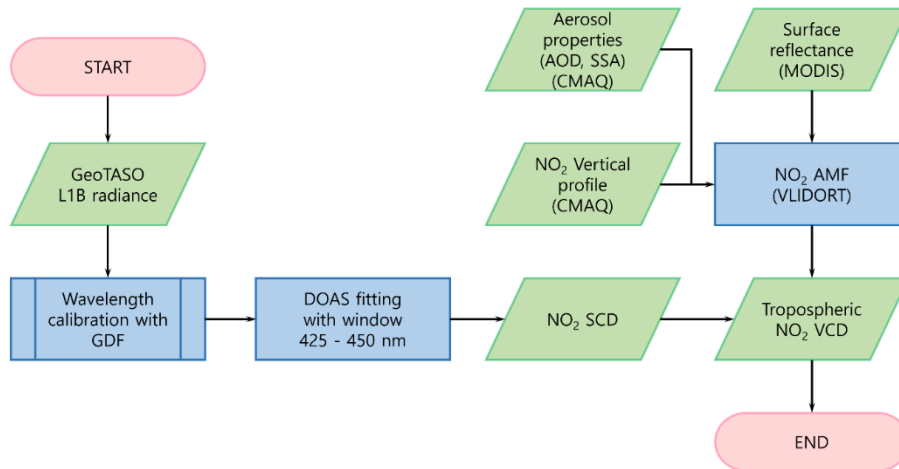
168 NO₂ VCDs were retrieved from the L1B radiance dataset (version: V02y) obtained using GeoTASO during the KORUS-AQ
 169 campaign. The NASA Goddard Space Flight Center conducted the L1B radiance calibration, which included offset and smear
 170 correction, gain matching, amplifier cross-talk correction, dark rate correction, integration normalisation, sensitivity derivation,
 171 wavelength registration, geo-registration, non-linearity correction, and ground pixel geolocation (Kowalewski et al., 2017;
 172 Chong et al., 2020). The detailed specifications of GeoTASO are listed in Table 2 (Nowlan et al., 2016).

173

174 **Table 2.** Summary for GeoTASO instrument and optical specification.

L1B version	V02y
Full cross-track field of view	45°
Single pixel cross-track field of view	0.046°
Wavelength	UV: 290–400 nm VIS: 415–695 nm
Spectral resolution (full width at half maximum, FWHM)	UV: ~0.39 nm VIS: ~0.88 nm
CCD	1,056 (wavelength) × 1,033 (cross-track)
Spatial resolution before binning	~35 m (along-track) × 7 m (cross-track)
Spatial resolution after binning	~250 m (along-track) × 250 m (cross-track)

175



176

177 **Figure 2.** Flowchart of the algorithm for retrieving tropospheric NO₂ data from GeoTASO.

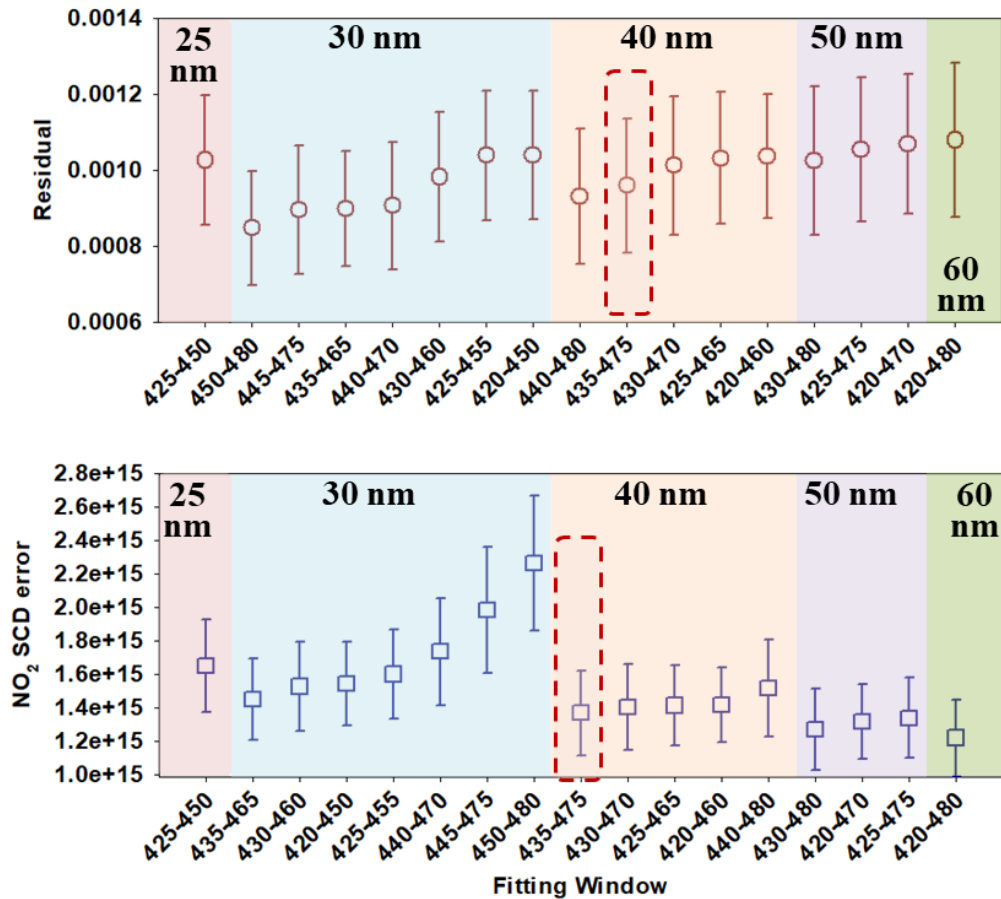
178

179 **2.4.1 NO₂ slant column density retrieval**

180 Figure 2 shows the flowchart for retrieving the tropospheric NO₂ VCD from the GeoTASO. We first retrieved NO₂ SCDs
 181 using the DOAS method (Platt, 1994). Nonlinear least square minimisation was used to retrieve the NO₂ SCDs which minimize
 182 the difference between the measured optical depth and the modelled value in QDOAS software (Eq. (1); Danckaert et al.,
 183 2012).

184
$$\frac{\ln I(\lambda)}{\ln I_0(\lambda)} = -(\sum_{j=1}^m \rho_j \times \sigma'_j(\lambda) + B(\lambda) + R(\lambda) + A(\lambda) + N(\lambda))$$
 (1)

185 Where $I(\lambda)$ is the measured earthshine radiance at wavelength λ ; I_0 is the reference radiance from the sea surface south of Jeju
 186 Island (red circle in Fig. 1, 32.983°N, 126.392°E) on 09 AM in 1 May 2016. The Community Multiscale Air Quality (CMAQ)
 187 modelling system data indicated that the NO_2 VCD from the surface to 50 hPa at this point on this day was 6.75×10^{15}
 188 molecules cm^{-2} (averaged NO_2 VCD obtained from OMI available during KOURS-AQ period is 4.77×10^{15} molecules cm^{-2}
 189 and standard deviation of 1.33×10^{15} molecules cm^{-2} , respectively); We confirmed the stability of NO_2 distribution in this
 190 region using TROPOMI offline data from 2019 to 2020. In this period the NO_2 VCD is 4.81×10^{15} molecules cm^{-2} and standard
 191 deviation of 0.43×10^{15} molecules cm^{-2} , respectively.
 192 ρ_j represents the SCD of each species j ; $\sigma'_j(\lambda)$ represents the differential gas phase absorption cross-section convolved with the
 193 Gaussian distribution function (GDF) with GeoTASO FWHM (the UV and VIS range were 0.34–0.49 nm and 0.70–1.00 nm,
 194 respectively (Nowlan et al., 2016)) at wavelength λ of species j , respectively.
 195

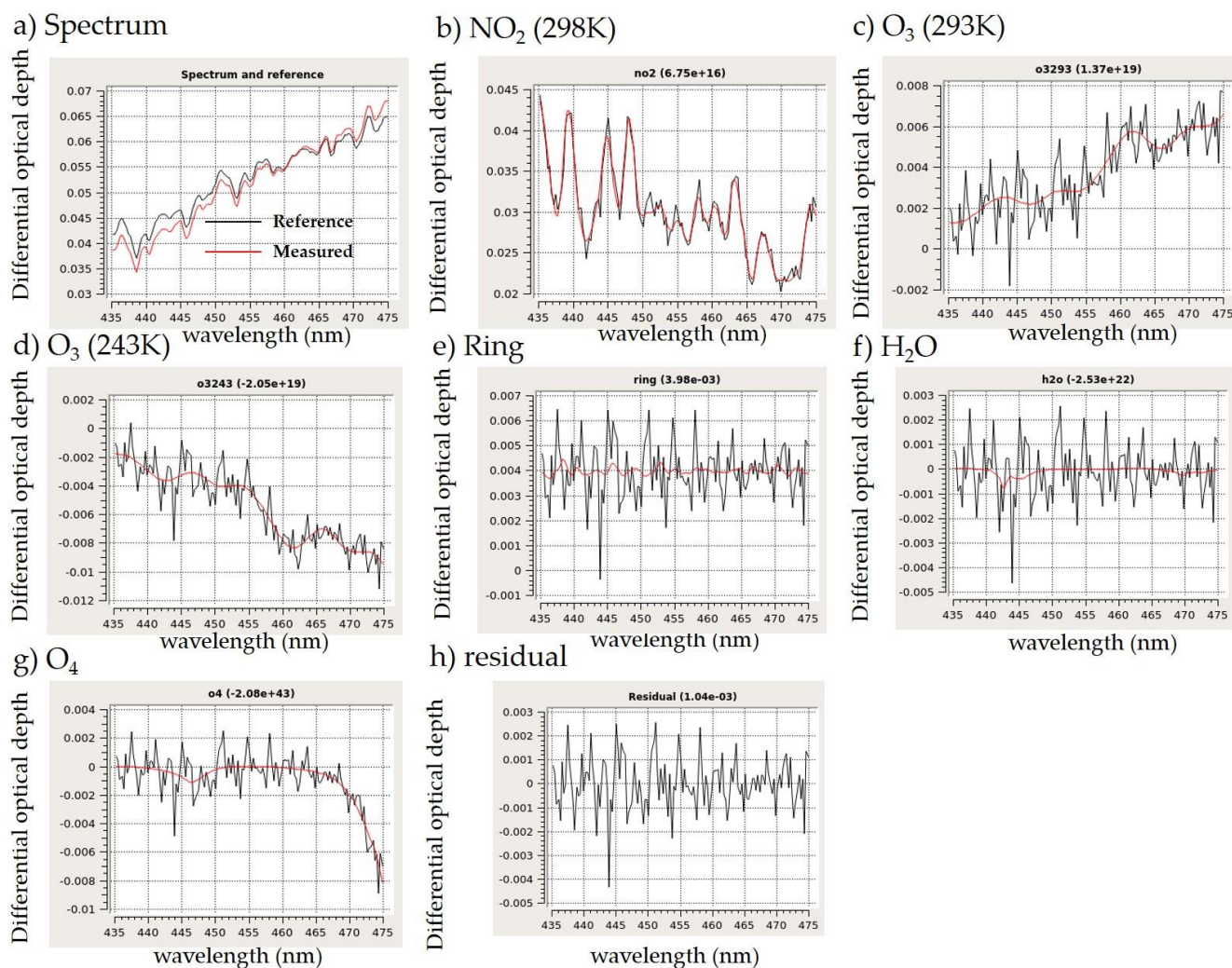


196
 197 **Figure 3. Residuals and NO_2 SCD errors of 17 spectral fitting window candidates (May 17, 2016, across track number: 15).**
 198

199 The spectral fitting window was selected based on the sensitivity test with 17 fitting window candidates from 420 nm to 480
 200 nm with the length of the fitting window from 25 nm to 60 nm. Spectral fitting residuals and NO_2 SCD errors have been
 201 investigated for 17 spectral fitting window candidates (Fig. 3).

202 In terms of the residual, when the NO_2 fitting window includes a wavelength region less than 430 nm, it tends to have a larger
 203 residual compared to the case where it does not. The higher residual can include the more noise signals that cannot be calculated
 204 mathematically, which can become an uncertainty for the NO_2 SCD retrievals. Therefore, we excluded the fitting window
 205 which includes wavelength less than 430 nm for the GeoTASO NO_2 retrievals during KORUS-AQ campaign. In case of NO_2
 206 SCD error, it was confirmed that the longer the fitting window length, the lower the NO_2 SCD error appeared regardless of
 207 including the wavelength region less than 430 nm. Therefore, for the stable NO_2 SCD retrieval, an appropriate spectral fitting
 208 window needs to be selected which can minimize the residual with a moderate length of the fitting window. To find the optimal

209 fitting window, we set the threshold value based on the results above: residual < 0.001 , NO_2 SCD error $< 1.4 \times 10^{15}$ molecules
 210 cm^{-2} , the length of fitting window > 30 nm. Then, the fitting window of 435–475 nm was finally selected for the GeoTASO
 211 NO_2 retrievals during KORUS-AQ campaign. To determine the wavelength registration more accurately in the narrow fitting
 212 window, additional wavelength calibration of the spectra for each of the 33 across track pixels was performed using a high-
 213 resolution solar reference spectrum (Kurucz solar spectrum) (Chance and Kurucz, 2010) with the GDF. The absorption cross-
 214 sections of NO_2 (Vandaele et al., 1998), O_3 (Bogumil et al., 2000), H_2O (Rothman et al., 2010), and the Ring effect as pseudo-
 215 absorbers (Chance and Spurr, 1997) were used to construct the model equation; and $B(\lambda)$, $R(\lambda)$, $A(\lambda)$, and $N(\lambda)$ are the broad
 216 absorption of the trace gases, extinction by Mie and Rayleigh scattering, variation in the spectral sensitivity of the detector or
 217 spectrograph, and noise, respectively, which were accounted by an 8th order polynomial. An example of the spectral fitting
 218 results is presented in Fig. 4.
 219



220
 221 **Figure 4.** An example of the spectral fitting results of NO_2 retrievals from GeoTASO during the KORUS-AQ campaign (at Gangnam,
 222 Seoul on 9 June, 2016). Red and black line in the panel (a) represent measured and reference spectrum, respectively. The panels
 223 from (b) to (h) depict examples of spectral fitting results of (b) NO_2 , (c) O_3 (293K), (d) O_3 (243K), (e) ring, (f) H_2O , (g) O_4 where red
 224 and black lines are absorption cross section of target species and the fitting residual plus the absorption of the target species,
 225 respectively. The panel (h) shows fitting residual of this example.

226

227 2.4.2 NO_2 AMF calculation

228 AMF, the ratio of SCD to VCD, can be calculated using the scattering weight (ω) and shape factor (S) (Palmer et al., 2001) in
 229 Eq. (2)–(5).

$$230 \quad AMF = \frac{SCD}{VCD} \quad (2)$$

$$231 \quad AMF = AMF_G \int_{z_1}^{z_2} \omega(z) S(z) dz \quad (3)$$

$$232 \quad \omega(z) = - \frac{1}{AMF_G} \frac{\partial \ln I_B}{\partial \tau} \quad (4)$$

$$233 \quad S(z) = \frac{\alpha(z)n(z)}{\int_{z_1}^{z_2} \alpha(z)n(z) dz} \quad (5)$$

234 Where AMF_G represents the geometric AMF, I_B is the earthshine radiance, τ is the optical depth, α is the absorption cross-
 235 section, and n is the number density of the absorber. NO_2 AMF was calculated using a linearised pseudo-spherical scalar and
 236 vector discrete ordinate radiative transfer model (VLIDORT, version 2.6; Spurr and Christi, 2014). Aerosol properties, such
 237 as AOD, SSA, and *a priori* NO_2 vertical profile information, were simulated using the CMAQ, and surface reflectivity was
 238 obtained from MODIS (Collection 6). The surface reflectance products, **MCD43A3, available at a 500 m spatial** resolution,
 239 provide an estimate of the surface spectral reflectance including MODIS bands 1 through 7. **Here, MODIS band 3 (459-479**
 240 **nm) was used, since this band is the closest the wavelength (455 nm) used in AMF calculation in this present study. At the**
 241 **pixels without reflectance information, AMF was not calculated.** The products were corrected for atmospheric conditions such
 242 as aerosol, gasses, Rayleigh scattering. In previous studies (Lamsal et al., 2017; Nowlan et al., 2018; Judd et al., 2019; Chong
 243 et al., 2020), an AMF were described for both above and below aircraft altitude is used to convert NO_2 SCDs to VCDs using
 244 Eq. (6)–(8).

$$245 \quad AMF \uparrow = AMF_G \int_{z_A}^{z_{TOA}} \omega(z) S(z) dz \quad (6)$$

$$246 \quad AMF \downarrow = AMF_G \int_{z_0}^{z_A} \omega(z) S(z) dz \quad (7)$$

$$247 \quad NO_2 \text{ VCD} \downarrow = \frac{NO_2 \text{ SCD} - AMF \uparrow \cdot NO_2 \text{ VCD} \uparrow}{AMF \downarrow} \quad (8)$$

248 Where $AMF \uparrow$ and $AMF \downarrow$ are AMF above and below aircraft, respectively, and $NO_2 \text{ VCD} \uparrow$ represents NO_2 VCD above the
 249 aircraft obtained from a chemical transport model (CTM). However, here we calculated $NO_2 \text{ VCD} \downarrow$ by dividing NO_2 SCDs
 250 by $AMF \downarrow$ because stratospheric and free tropospheric NO_2 ($NO_2 \text{ VCD} \uparrow$) column densities are much lower than tropospheric
 251 NO_2 column densities, especially in megacities and industrial areas (Valks et al., 2011). **However, in this case, NO_2 present in**
 252 **the stratosphere could not be removed, it was hard for us to consider the temporal variation of NO_2 in stratosphere in this**
 253 **present study.**

254

255 2.5 Chemical model description

256 Vertical profiles from CMAQ (Byun and Ching, 1999; Byun and Schere, 2006), a CTM, were used to calculate AMFs. CMAQ
 257 simulations were conducted with a horizontal resolution of 15×15 km and had 27 vertical layers from the surface to 50 hPa.
 258 The meteorological fields were prepared using the advanced research Weather Research and Forecasting (WRF)-Advanced
 259 Research WRF (ARW) Model (Skamarock et al., 2008). Anthropogenic emissions were generated based on the KORUS v5.0
 260 model (Woo et al., 2012), and biogenic emissions were simulated using the Model of Emissions of Gases and Aerosols from
 261 Nature (MEGAN v2.1; Guenther et al., 2006; 2012). Besides anthropogenic and biogenic emissions, the Fire Inventory from
 262 NCAR (FINN; Wiedinmyer et al., 2006, 2011) was utilised to update the pyrogenic emission fields.

263 CMAQ AOD was calculated by integrating the aerosol extinction coefficient (Q_{ext}), which is the sum of scattering (Q_{sca}) and
 264 absorption (Q_{abs}) coefficients, over all vertical layers (z) as follows:

$$265 \quad AOD = \int Q_{ext}(z) dz = \int \{Q_{sca}(z) + Q_{abs}(z)\} dz \quad (9)$$

$$266 \quad Q_{abs} [Mm^{-1}] = \sum_i \sum_j \{ (1 - \omega_{ij}) \cdot \beta_{ij} \cdot f_{ij}(RH) \cdot [C]_{ij} \} \quad (10)$$

$$267 \quad Q_{sca} [Mm^{-1}] = \sum_i \sum_j \{ \omega_{ij} \cdot \beta_{ij} \cdot f_{ij}(RH) \cdot [C]_{ij} \} \quad (11)$$

268 Here, ω_{ij} indicates SSA of particulate species i for the particulate mode (or size bin) j , β_{ij} denotes the mass extinction
 269 efficiency, $f_{ij}(RH)$ is the hygroscopicity factor according to the relative humidity (RH), and $[C]_{ij}$ is the concentration of
 270 particulate species. CMAQ SSA is defined as the ratio of the integrated Q_{sca} to AOD, and NO_2 vertical profiles were obtained
 271 from NO_2 concentrations at each vertical layers by conducting CMAQ simulations. Details of the model descriptions and
 272 calculations of optical properties are given in Lee et al. (2020) and Malm and Hand (2007).

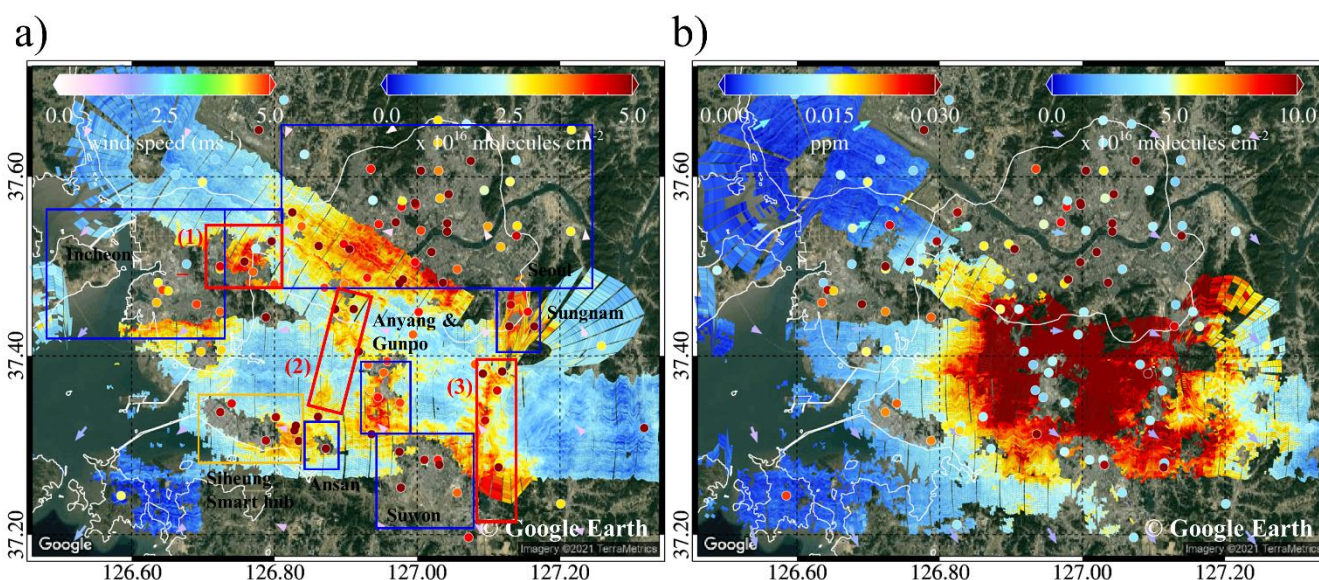
273 3 Results and discussion

274 3.1 NO_2 VCD retrieval

275 3.1.1 Seoul metropolitan region

276 We showed the finally NO_2 VCDs from 250 m spatial resolution. As the results of NO_2 VCD, we selected the dates observed
 277 in both the morning and afternoon during the KORUS-AQ period over Seoul metropolitan area, Busan, and Anmyeon. The
 278 retrieved dates for NO_2 VCDs were 5, 9, and 10 Jun, 2016.

279 The population of the Seoul metropolitan region is approximately 20 million, which is approximately 40% of the total
 280 population of South Korea. It is very rare to obtain high-resolution horizontal NO_2 VCD distributions using airborne
 281 measurements in the morning and afternoon, especially in Asian megacities. Fig. 5 shows tropospheric NO_2 VCDs over Seoul
 282 on 9 June 2016, at 9 AM and 3 PM local time (LT).



283 **Figure 5.** Tropospheric NO_2 VCD, in the Seoul metropolitan region on 9, June 2016 retrieved from GeoTASO: a) at 9 AM and b) at
 284 3 PM. The red boxes represent expressways (counterclockwise from left to right, (1) Gyeongin expressway, (2) Seohaean expressway,
 285 and (3) Gyeongbu expressway), the orange box indicates the industrial complex, and the blue boxes indicate the major cities (Seoul,
 286 Incheon, Suwon, Bucheon, Anyang, Gunpo, Sungnam, and Ansan) of the Seoul metropolitan region. Colours of the circles depict
 287 the NO_2 surface mixing ratio obtained from Air-Korea. The colour arrows show the wind direction and speed at 1000 hPa over Seoul
 288 metropolitan region, obtained via the Unified Model (UM) simulations (background RGB image is from Google Earth;
 289 <https://www.google.com/maps/>).

291
 292 In the morning, NO_2 VCDs retrieved from GeoTASO were highly correlated with expressways (red boxes in Fig. 5), such as
 293 the Gyeongin, Seohaean, and Gyeongbu Expressways, and over major cities with heavy traffic, such as Seoul, Bucheon, Ansan,
 294 Anyang, and Suwon. GeoTASO observed NO_2 VCD values three-times higher ($>3 \times 10^{16}$ molecules cm^{-2}) in these areas
 295 compared to the surrounding rural areas. In particular, high NO_2 VCD values above 6×10^{16} molecules cm^{-2} were observed
 296 above the Gyeongin Expressway, which has very heavy traffic in a relatively short section, and the Gunpo Complex Logistics
 297 zone, where diesel vehicle traffic is also high. The major NO_2 source regions and the regions where high NO_2 VCD values

298 were observed were highly consistent at 9 AM because the wind speed at this time—as obtained from the unified model (UM)
 299 based Regional Data Assimilation and Prediction System (RDAPS) of the Korea Meteorological Administration (KMA)—
 300 was as low as 0.1 ms⁻¹ and the average wind direction was 84.7° at 1000 hPa over Seoul metropolitan region. The average
 301 daily traffic volume of these expressways exceeds 150,000 vehicles, and the total number of vehicles registered in these major
 302 cities is > 6,000,000, with an average daily mileage per car per day of over 38 km. Detailed information on these cities and
 303 expressways is listed in Table 3 and Table 4. Based on the level of vehicular traffic, combustion using gasoline and diesel
 304 engines leads to high overall emissions of NO₂ in the Seoul metropolitan region (Kendrick et al., 2015).

305

306 **Table 3.** The population, number of registered vehicles, and average mileage per car per day of major cities in the Seoul and
 307 **Busan** metropolitan region obtained from the Korean Statistical Information Service (<https://kosis.kr/eng>).

City	Population (millions)	Vehicle registration number (thousands)	Average mileage (km car ⁻¹ day ⁻¹)
Seoul	9.776	3,083	37.1
Incheon	2.914	1,402	41.7
Bucheon	0.848	284	37.2
Ansan	0.744	289	40.8
Anyang	0.596	206	39.6
Gunpo	0.286	87	38.8
Suwon	1.241	467	38.1
Sungnam	0.994	358	36.3
Busan	3.389	1,295	40.1
Daegu	2.450	1,121	37.1
Changwon	1.080	551	37.5
Kimhae	0.529	250	38.0

308

309 **Table 4.** Daily average traffic volume on the Gyeongin, Gyeongbu, and Seohaean Expressways obtained using the Traffic
 310 Monitoring System (<https://www.road.re.kr>).

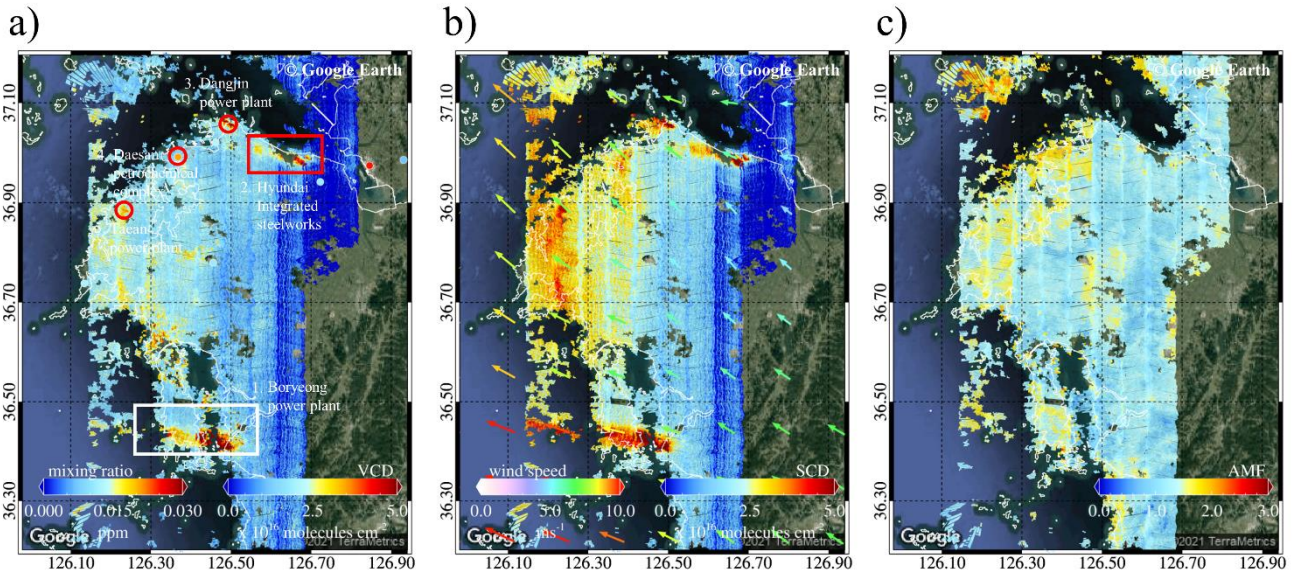
Expressway	Daily average traffic volume
Gyeongin Expressway	162,369
Gyeongbu Expressway	173,413
Seohaean Expressway	150,298

311

312 Compared the data from the morning, the average wind speed and wind direction were 1.7 ms⁻¹ and 284.5° at 1000 hPa in the
 313 afternoon and the afternoon had extremely high tropospheric NO₂ VCD values (exceeding 5 × 10¹⁶ molecules cm⁻²) in most of
 314 the Seoul metropolitan regions including rural areas, whereas the NO₂ mixing ratio (MR) obtained from Air-Korea decreases
 315 in the afternoon. According to Tzortziou et al. (2018), similar results were retrieved from the Pandora site in Seoul, with higher
 316 afternoon NO₂ VCDs than in the morning. This result is presumed to be due to the reason that the amount of NO₂ produced by
 317 chemical conversion of nitric oxide (NO) by O₃ and VOCs in the atmosphere, along with NO_x generated by regional emissions
 318 (traffic) in the Seoul metropolitan region, is greater than the amount lost by photolysis and transport to nearby areas (Herman

319 et al., 2018). In addition, the increase in tropospheric NO₂ VCD in the afternoon is presumed to be due to the accumulation
 320 and dispersion of NO₂ according to the change in the planetary boundary layer height (Ma et al., 2013).

321 3.1.2 Industrial and power plant regions in Anmyeon



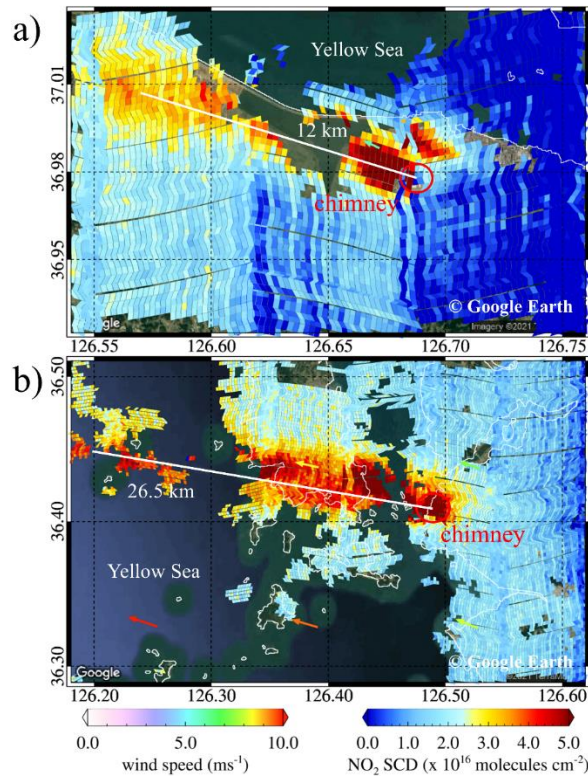
322
 323 **Figure 6.** a) Tropospheric NO₂ VCD and b) NO₂ SCD retrieved from GeoTASO, and c) NO₂ AMF, native resolution (250 m)
 324 calculated using VLIDORT over Anmyeon in South Korea on 5 June 2016. The colored arrows indicate wind speed and wind
 325 direction at 850 hPa from the Unified Model (UM) simulations. The red circles and rectangle in panel (a) represent the major NO₂
 326 emission sources, such as steelworks and power plants (background RGB image is from Google Earth;
 327 <https://www.google.com/maps/>).

328
 329 The high spatial resolution of tropospheric NO₂ VCD from GeoTASO over the Anmyeon industrial region, where many
 330 industrial facilities and several power plants are distributed, is shown in Fig. 6. The panels a and b of this figure show the
 331 binned tropospheric NO₂ VCD and NO₂ SCD retrieved from GeoTASO L1B data, respectively, between 13:00 and 17:00 LT
 332 on 5 June 2016. The panel c depicts the calculated AMF of NO₂ from native resolution over the domain. The GeoTASO
 333 observations clearly detected moderate and strong NO₂ emission sources over this area: (1) Boryeong power plant, (2) the
 334 Hyundai integrated steelworks, (3) Dangjin power plant, (4) the Daesan Petrochemical Complex, and (5) Taean power plant.
 335 High NO₂ VCD values ($> 5 \times 10^{16}$ molecules cm⁻²) were observed over steel mill works, petrochemical complexes, and power
 336 plants, whereas values were comparatively low ($< 1 \times 10^{16}$ molecules cm⁻²) over small cities including Seosan, Dangjin, and
 337 Boryeong with populations of less than 0.1 million, and the Seohaean Expressway. In 2016, the annual NO_x emissions by the
 338 Hyundai steelworks and the Dangjin and Boryeong power plants were about 10.3, 11.9, and 16.8 kt year⁻¹, respectively. NO₂
 339 emission rates from major industrial facilities in the Anmyeon region are shown in Table 5.

341 **Table 5.** NO₂ emission rates in 2016 from major industrial facilities in the Anmyeon region obtained from the Continuous
 342 Emission Monitoring System of the Korea Environment Corporation (<https://www.stacknsky.or.kr/eng/index.html>).

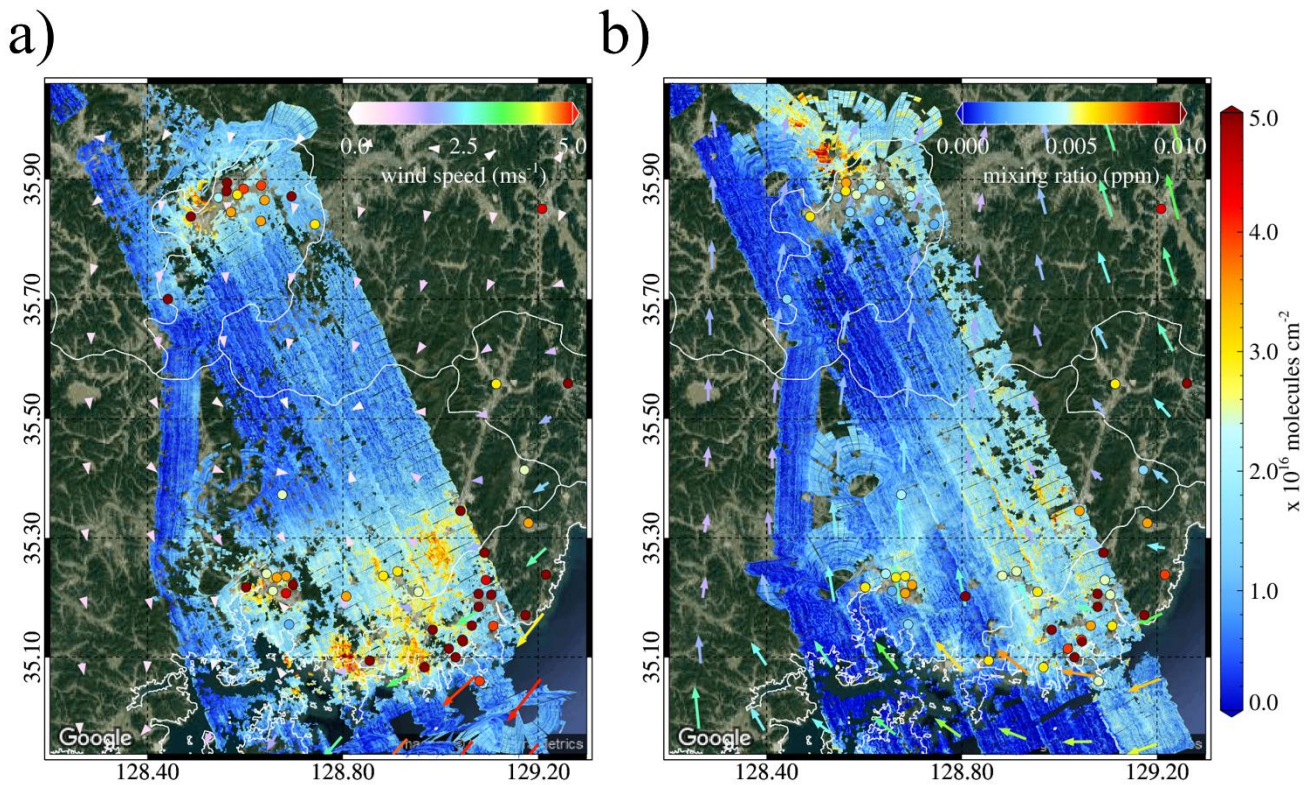
Industrial facilities	NO ₂ emission rate (kg year ⁻¹)
Boryeong power plant	16,788,438
Hyundai integrated steelworks	10,271,075
Dangjin power plant	11,852,972
Daesan petrochemical complex	3,397,939

344 Figure 6 shows high NO₂ concentrations of major industrial facilities in the Anmyeon region, where fossil fuel combustion in
 345 factories and thermal power plants leads to high emissions (Prasad et al., 2012). Due to relatively sparse distribution over rural
 346 areas, the Air-Korea measurements did not detect the major NO₂ plume as shown in Fig. 6a. Thus, airborne remote sensing
 347 systems, such as GeoTASO, can effectively compliment the ground-based networks for monitoring minor and major NO₂
 348 emissions, particularly over these remote industrial regions.



349
 350 **Figure 7.** Enlarged view of GeoTASO tropospheric NO₂ VCD observation over a) Hyundai steel works, indicated by the red box in
 351 Figure 6, and b) the Boryeong power plant, indicated by the white box in Figure 6. The arrows represent the wind direction and
 352 speed at 850 hPa from the Unified Model (UM) simulations, respectively (background RGB image is from Google Earth;
 353 <https://www.google.com/maps/>).

354
 355 The GeoTASO data captured not only NO₂ emissions from the chimneys of steelworks and power plants but also its transport
 356 by the wind. Fig. 7a and 7b show enlarged views of tropospheric NO₂ SCD retrieved using GeoTASO over the Hyundai
 357 steelworks (red box in Fig. 6) and the Boryeong power plant (white box in Fig. 6). The arrows in Fig. 7 represent the prevailing
 358 wind direction and speed from RDAPS. NO₂ emitted from the chimneys of these sites was transported to the Yellow Sea,
 359 travelling distances of over 26.5 km at speeds of approximately 6 ms⁻¹. According to Chong et al. (2020), similar results were
 360 found for SO₂ emitted and transported from these sites.



362

363 **Figure 8.** Tropospheric NO₂ VCD in the Busan metropolitan region in the (a) morning and (b) afternoon of 10 June 2016. The
 364 wind speed (colours scale) and wind direction (arrows) at 1000 hPa pressure level were obtained from the Unified Model (UM)
 365 simulations. The white boxes represent major cities such as Busan, Daegu, Changwon, and Kimhae. The orange box
 366 represents Busan Newport (background RGB image is from Google Earth; <https://www.google.com/maps/>).

367

368 **Fig. 8a and 8b** show tropospheric NO₂ VCD retrieved from the GeoTASO L1B data over the Busan metropolitan region on 10
 369 June 2016 in the morning (between 08:00 and 11:00 LT) and afternoon (between 13:00 and 16:00 LT), respectively. The
 370 arrows in Fig. 8 show the wind speed and wind direction of 1000 hPa obtained from the UM-RDAPS, with the average wind
 371 speed and wind direction of 0.9 ms⁻¹ and 55.4°, 1.9 ms⁻¹ and 147.0°, respectively, in the morning and afternoon. High NO₂
 372 VCDs were observed above urban areas, the port, industrial complexes, and the inter-city road between Busan and Changwon.
 373 Similar to the Seoul metropolitan regions, it is estimated that combustion using gasoline and diesel engines contributes to the
 374 high NO₂ emission. In the morning, NO₂ VCDs were high (approximately 3×10^{16} molecules cm⁻²) in the major cities and,
 375 especially, around Busan Newport, with values exceeding 7×10^{16} molecules cm⁻². In comparison, in the mountainous regions
 376 between Daegu and Busan, NO₂ VCD values were less than 1×10^{16} molecules cm⁻² during the same period. The spatial
 377 distribution of tropospheric NO₂ VCDs was similar to that in the Seoul metropolitan regions, with high values over major cities
 378 and roads (compare Figs. 5 and 8). In Busan, fossil fuel combustion using both road vehicles and ships likely contributes to
 379 the NO₂ emissions. In the afternoon, unlike Seoul metropolitan region, tropospheric NO₂ VCD over Busan decreased by over
 380 3×10^{16} molecules cm⁻², which also corresponds with NO₂ MR data obtained from the Air-Korea sites. Detailed information
 381 on these cities is listed in Table 3.

382

383 3.2 Error estimation

384 NO₂ VCD retrieval accuracy using the DOAS method depends on both the AMF calculation and spectral fitting error of the
 385 SCD retrieval. Retrieval errors of the NO₂ VCD were estimated using error propagation analysis as expressed in Eq. (12).

$$\frac{\varepsilon_{VCD}}{VCD} = \sqrt{\left(\frac{\varepsilon_{SCD}}{SCD}\right)^2 + \left(\frac{\varepsilon_{AMF}}{AMF}\right)^2} \quad (12)$$

Where ε_{VCD} is the total error of NO₂ VCD. The error of NO₂ SCD (ε_{SCD}) is obtained from the spectral fitting error of NO₂ SCD via DOAS spectral fitting. ε_{AMF} indicates the error of NO₂ AMF caused by uncertainties in the model input parameters for AMF calculation. Uncertainties in aerosol properties (AOD, SSA, and ALH) and surface reflectance for the RTM calculations are known to be the major factors affecting NO₂ AMF accuracy (Boersma et al., 2004; Leitão et al., 2010; Hong et al., 2017). Therefore, in this present study, we quantified the NO₂ AMF errors (ε_{AMF}) due to uncertainties in the input parameters independent of one another using Eq. (13):

$$\varepsilon_{AMF} = \sqrt{\left(\frac{\partial AMF}{\partial AOD}\right)^2 \sigma_{AOD}^2 + \left(\frac{\partial AMF}{\partial SSA}\right)^2 \sigma_{SSA}^2 + \left(\frac{\partial AMF}{\partial ALH}\right)^2 \sigma_{ALH}^2 + \left(\frac{\partial AMF}{\partial SFR}\right)^2 \sigma_{SFR}^2} = \sqrt{\sum_{i=1}^4 \left(\frac{\partial AMF}{\partial \chi_i}\right)^2 \sigma_{\chi_i}^2}, \quad (13)$$

where $\frac{\partial AMF}{\partial \chi_i}$ are partial derivatives of NO₂ AMF with respect to the input parameters (χ_i), σ_{χ_i} represents the uncertainty of the χ_i . The σ of AOD, SSA, surface reflectance, and ALH are assumed as 30% (Ahn et al., 2014), 0.04 (Jethva et al., 2014), (0.005+0.05×surface reflectance; EOS Land Validation; <https://landval.gsfc.nasa.gov>), and 1 km (Fishman et al., 2012), respectively, in this study. To derive $\left(\frac{\partial AMF}{\partial \chi_i}\right)^2$, the true χ_i is input to the RTM to simulate ‘true’ NO₂ AMF. For the AOD, SSA, ALH, and surface reflectance (SFR), perturbed NO₂ AMF was simulated using RTM with $\chi_i \pm \sigma_{\chi_i}$. $\partial \chi_i$ denotes the difference between the ‘centre’ χ_i and $\chi_i \pm \sigma_{\chi_i}$, and ∂AMF is the difference between the ‘centre’ NO₂ AMF (AMF_{centre}) simulated with ‘centre’ input values and the perturbed NO₂ AMF (AMF_{perturbed}) simulated using the perturbed input parameters $\chi_i \pm \sigma_{\chi_i}$ (i.e. the original input parameters modified by the uncertainty). The simulation for calculating the ε_{AMF} was conducted using the input parameters on 9 June 2016.

403

404 **Table 6.** Total errors of NO₂ VCD caused by uncertainties in NO₂ SCD and NO₂ AMF (the average for the flight on 9 June
405 2016).

	AOD	2.8%
	SSA	4.1%
NO ₂ AMF errors	Aerosol loading height	22.3%
	Surface reflectance	2.8%
	Total NO₂ AMF error due to aerosol uncertainties	23.3%
	NO ₂ SCD error	11.7%
	NO₂ VCD error	26.9%

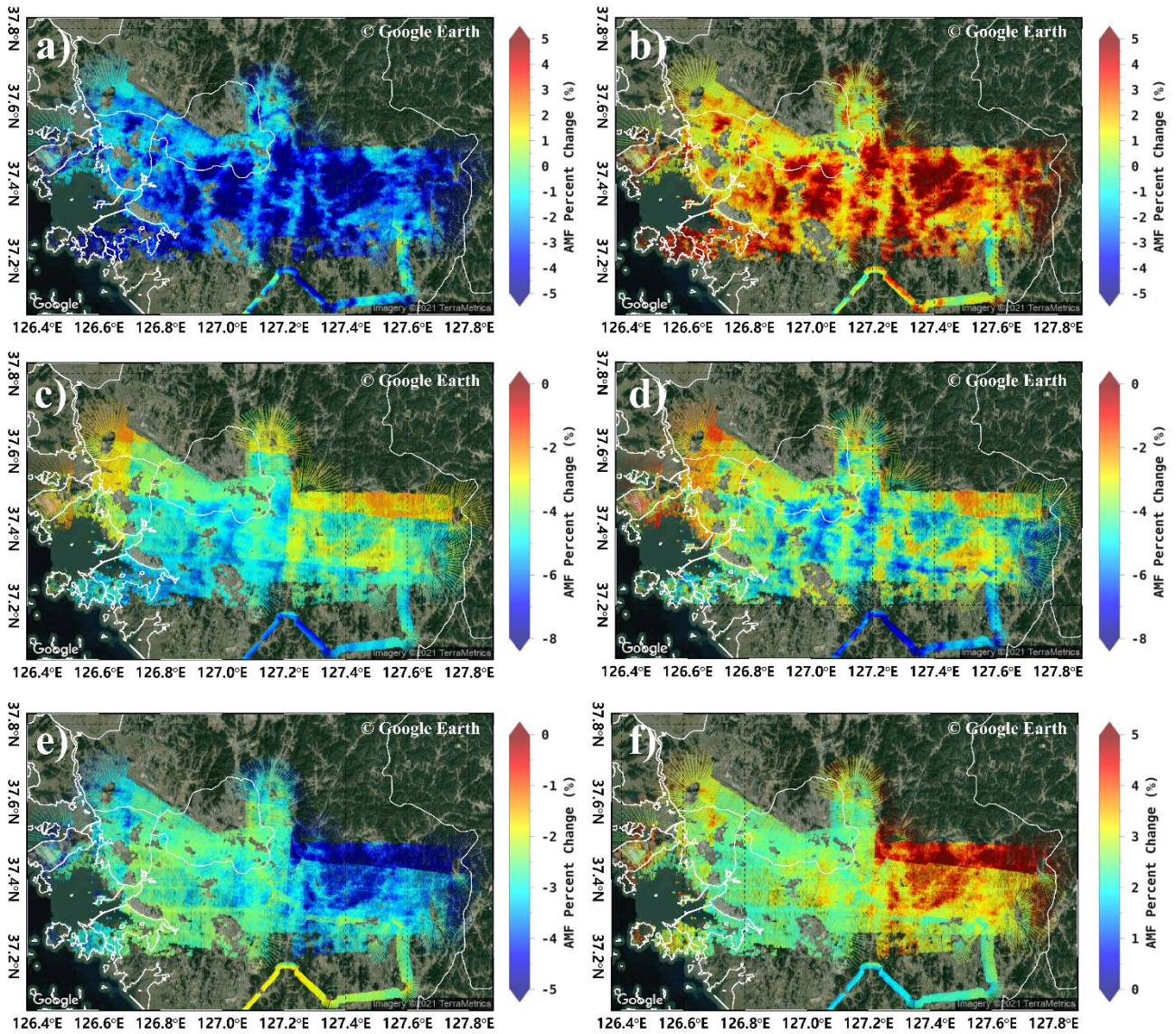
406

407 Table 6 lists the estimated NO₂ VCD error on 9 June 2016 for each sources based on the error propagation method. The error
408 estimation was conducted for the pixels where root mean square residual < 0.001 and NO₂ VCD > 5 × 10¹⁵ molecules cm⁻²
409 since NO₂ SCD precision is reported to be highly decreased in low NO₂ conditions (Hong et al., 2017). The total NO₂ VCD
410 error was 26.9% with a high portion of NO₂ AMF error. The NO₂ SCD error was calculated to be 11.7%, showing the
411 importance of accurate DOAS spectral fitting to derive NO₂ SCD. The total AMF error due to uncertainties in input parameters
412 was calculated to be 23.3%. Among model input parameters, the effect of ALH on NO₂ AMF become highest (22.3%),
413 indicating importance of accurate aerosol profile information. ALH sensitively affects NO₂ AMF because near the surface

414 where trace gases and aerosols are well mixed, aerosols lead to multiple scattering effects and the light absorption of trace
 415 gases due to increasing light path (Castellanos et al., 2015; Hong et al., 2017). Especially, ALH can be the most important
 416 input parameter in the Asia region where high loadings of aerosol plumes persist throughout the year. The NO₂ AMF
 417 calculation errors due to uncertainties in SSA and AOD were 4.1% and 2.8%, respectively. The NO₂ AMF calculation error
 418 due to uncertainties in aerosol optical properties (SSA and AOD) seems smaller than those in the previous study (Leitão et al.,
 419 2010). The smaller effect of aerosol properties can be explained by the moderate aerosol loading (AOD = 0.40) on the flight
 420 day. It is expected that NO₂ AMF errors become larger under high AOD condition. The smallest effect of SRF was found on
 421 NO₂ AMF calculation error. A priori NO₂ profile shape also can be one of factors to cause calculation error for NO₂ AMF as
 422 reported in the previous studies (Leitao et al., 2010, Meier et al., 2016, Hong et al., 2017). It is necessary to calculate the effect
 423 of a priori NO₂ profile shape on the accuracy of NO₂ AMF in the future. Moreover, the resulting uncertainties of input
 424 parameters of a GeoTASO ground pixel need to be considered by combining the initial uncertainties of CTM and satellite-
 425 based products, and by the variability of the parameters within the respective CTM (AOD, SSA, and ALH) and satellite (SFR)
 426 grid box. If values such as surface reflectance are assumed constant over larger areas, the fundamental spatial variability in
 427 this input data increases the uncertainty of the AMF and hence of the determined NO₂ VCD on the respective finer spatial
 428 scale. This kind of analysis should be taken into account in further study.

$$429 \quad AMF_{percent_change} = \frac{AMF_{perturbed} - AMF_{centre}}{AMF_{centre}} \times 100 \quad (14)$$

430



431

432 **Figure 9.** Percent **change** between AMF calculated using the CMAQ model simulation and those using a) 30% lower AOD,
 433 b) 30% higher AOD, c) 0.04 lower SSA, d) 1km higher ALH, compared to the model outputs. The percent **change** for AMF
 434 calculated using MODIS data and those using e) 20% $0.005 + 0.05 \times \text{SFR}$ lower SFR, f) $0.005 + 0.05 \times \text{SFR}$ higher SFR
 435 (background RGB image is from Google Earth; <https://www.google.com/maps/>).

436

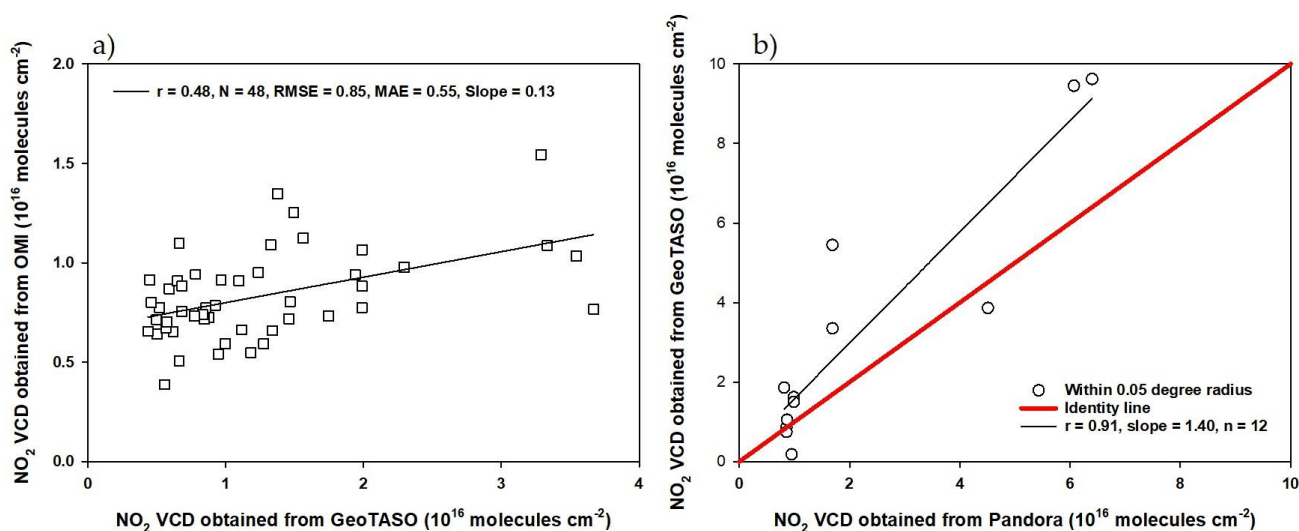
437 In this present study, we additionally investigated the spatial distribution of AMF calculation errors associated with
 438 uncertainties in aerosol properties (AOD, SSA, ALH, and SFR). Percent **change** of NO_2 AMF ($\text{AMF}_{\text{percent_change}}$) was calculated
 439 on each spatial pixel using Eq. (14). Fig. 9a and 9b show the percent **change** error between the calculated AMFs using the
 440 CMAQ AOD data with 30% lower (Fig. 9a) and 30% higher (Fig. 9b) values, respectively. The AMF decreased and increase
 441 by up to 10% with decreasing and increasing AOD, respectively, in the Seoul metropolitan region. We estimated that, under
 442 low aerosol loading conditions, an increase in AOD near the surface leads to an increase in the scattering probability within
 443 the surface layer with high NO_2 concentrations. Fig. 9c shows the percent **change** error between the calculated AMFs using
 444 CMAQ SSA data with a 0.04 lower value. The AMF decreased with decreasing SSA because the absorption of light increased.
 445 The ALH was also found to highly affect the accuracy of the AMF calculations (Fig. 9d). The ALH uncertainty of 1 km
 446 decreased AMFs with average $\text{AMF}_{\text{percent_change}}$ of -25% on the flight day. Especially, on the pixels where $\text{AOD} > 0.6$, the
 447 average $\text{AMF}_{\text{percent_change}}$ was found to be -26% while that was -27% on the pixels where $\text{AOD} < 0.4$, showing the combined
 448 effect of aerosol loading and aerosol profile shape on the NO_2 AMF calculations. Fig. 9e and 9f show the percentage **change**

449 error between the calculated AMFs using the MODIS surface reflectance data with $0.005 + 0.05 \times \text{SFR}$ lower (Fig. 9e) and
450 $0.005 + 0.05 \times \text{SFR}$ higher (Fig. 9f) values, respectively. The AMF decreased by about 3% when surface reflectance decrease,
451 and vice versa when it increased.

452 3.3 Validation of NO₂ VCDs retrieved from GeoTASO

453 Tropospheric NO₂ VCDs retrieved from GeoTASO L1B data (NO_{2,G}) were compared with those obtained from OMI NO₂
454 VCDs (NO_{2,O}) and Pandora (NO_{2,P}). The NO_{2,O} were only available for 10 June during the campaign period. Therefore, we
455 only compared 48 NO_{2,G} and NO_{2,O} data points within a radius of 20 km and 30 min, which yielded a correlation coefficient
456 of 0.48 with a slope of 0.13 (Fig. 10 a)). In order to validate, All NO_{2,G} within a radius 20 km of the OMI center coordinate
457 were averaged.

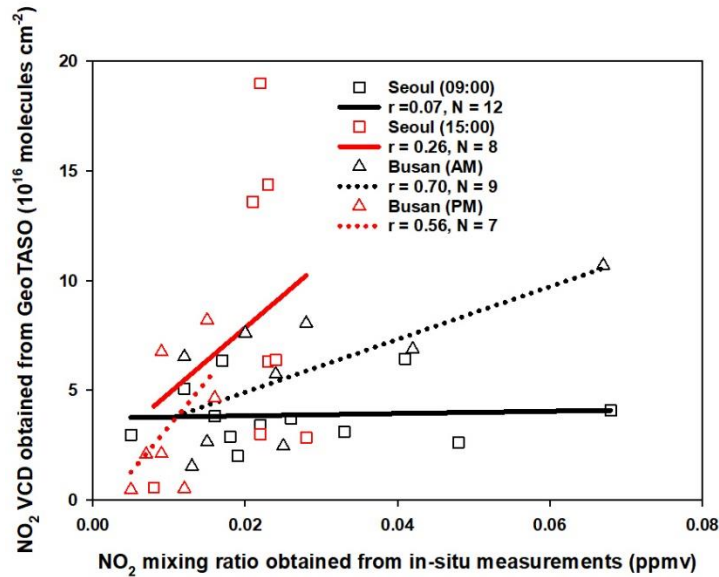
458 The NO₂ values are relatively low since GeoTASO observation is carried out in a region with low NO₂ compared to Seoul
459 metropolitan and the overpass time of OMI is about 13:30 LT when NO₂ decreased. It is thought that the reason the low slope
460 value is because the OMI with low spatial resolution does not reflect the spatial NO₂ inhomogeneity in the pixel.



461
462 **Figure 10.** Scatter plots of a) NO₂ VCD retrieved from GeoTASO and those obtained from OMI and b) NO₂ VCD obtained from
463 Pandora and those retrieved from GeoTASO, respectively.

464
465 To compare NO_{2,G} data, we made a comparison with NO₂ VCD obtained from the Pandora system (NO_{2,P}) during the KORUS-
466 AQ campaign period. NO_{2,P} obtained from Busan University, Olympic Park, Songchon, Yeosu, and Yonsei University Pandora
467 sites on June 5, 9, and 10 were used for the GeoTASO validation (Fig. 1). NO_{2,G} and NO_{2,P} columns at these sites are compared
468 in Fig. 11. In order to compare NO_{2,G} and NO_{2,P}, we used averaged NO_{2,G} retrieved from 16 across track with smallest viewing
469 zenith angle and averaged 30 min NO₂ obtained from pandora measurement within a radius of approximately 0.05 degree.
470 NO_{2,G} and NO_{2,P} were correlated ($R = 0.91$, with a slope of 1.40), however, when NO_{2,P} was lower than 1×10^{16} molecules
471 cm^{-2} , the correlation coefficient between NO_{2,G} and NO_{2,P} was < 0.1 . The weak correlation at low NO₂ levels are most likely
472 to reflect the differences in viewing geometries and the horizontal inhomogeneity of the measured NO₂ between Pandora and
473 GeoTASO. Also, from this result, it is thought that it can be used for NO₂ validation of geostationary satellite such as GEMS
474 using Pandora and GeoTASO. However, since the number of pandora is limited in this campaign, we had difficulties to validate
475 NO₂ retrieved from GeoTASO under various conditions. We believe that many ground-based remote sensing measurements
476 are needed to validate GEMS under various conditions.

477
478
479



481

482 **Figure 11.** Scatter plot of the NO₂ VCDs retrieved from GeoTASO, and NO₂ surface mixing ratio obtained from Air-Korea.
 483 The black and red squares represent the NO₂ data at 9 AM and 3 PM (local time) over the Seoul metropolitan region,
 484 respectively. The black and red triangles represent those in the morning and afternoon, over Busan, respectively.

485

486 To compare the spatiotemporal distribution of NO₂ VCDs retrieved from GeoTASO, NO_{2,G} in comparisons to surface spatial
 487 patterns, NO_{2,G} was compared with NO_{2,A} for GeoTASO data within a radius of approximately 0.05 km and 30 min (Fig. 11).

488 In order to compare NO_{2,G} and NO_{2,A}, we used averaged NO_{2,G} retrieved from 16 across track and averaged 30 min within a
 489 radius of 0.05 degree. Since in-situ measurements provides NO₂ VMR (NO_{2,A})(ppmv) once per hour, NO_{2,A} of the nearest time

490 is used to compare with NO_{2,G}. The correlation coefficient (R) between NO_{2,G} (molecules cm⁻²) and NO_{2,A} at 9 AM and 3 PM
 491 LT in the Seoul metropolitan region was 0.07 and 0.26, respectively. When using only roadside station data from Air-Korea,

492 the R-value for the morning increased to 0.72, which implies GeoTASO is more sensitive to emissions from NO₂ source areas,
 493 such as roadsides (Fig. 5). As a result of the comparison, there were large differences in the morning and afternoon. These

494 results were identified because synoptic meteorology played an important role from June 1 to June 10, 2016 (Choi et al., 2019).
 495 As described by Judd et al. (2018), the spatial distribution for NO₂ VCDs appears that reflects the emission source in local

496 industrialized regions and transportations in the morning with relatively weak winds. In general, NO₂ concentration increases
 497 to late morning, indicating that the emissions process proceeds faster than the NO₂ removal process. As the planetary boundary

498 layer heights (PBLH) in early afternoon increase and surface NO₂ is mixed through a deeper PBLH, the NO₂ VCDs distribution
 499 showed a wider increase in most of the Seoul metropolitan area and the overall column amounts continue to increase (Judd et

500 al., 2018).

501 In addition, when comparing NO₂ VCDs with surface NO₂ concentrations, it should be interpreted carefully that it is a non-
 502 linear relationship between NO_{2,G} and NO_{2,A}. Although it may vary depending on weather conditions, high NO₂ VCDs from

503 airborne observations may sometimes be detected with low surface NO₂ concentrations. In particular, when exhaust gases
 504 emitted from industrial facilities are happen at a certain altitude (stacks/chimneys), NO_{2,G} show high NO₂ VCDs, but NO_{2,A}

505 may be observed to have a low concentration. Unfortunately, in Anmyeon industrial region, NO_{2,G} and NO_{2,A} could not be
 506 compared due to spatial restrictions because the distribution of ground observation stations is concentrated in metropolitan

507 areas.

508 In the Busan metropolitan area, the R-value of the NO_{2,G} and NO_{2,A} data had a correlation coefficient greater than 0.56. This
 509 reflects the more even horizontal distribution of NO₂ in the afternoon, when diffusion from the source areas had taken place.

510 However, for a more accurate comparison, NO₂ VCD data should be converted to NO₂ MR based on mixing layer height,

511 temperature, and pressure profile data (Kim et al., 2017; Qin et al., 2017; Jeong and Hong, 2021a). However, since the number
512 of pandora and satellite data is limited in this campaign, we had difficulties to validate NO₂ retrieved from GeoTASO under
513 various conditions. Since ground-based, airborne and space borne remote sensing measurements has their own advantage and
514 disadvantage, I believe that a comprehensive observation campaign involving all of ground-based, airborne and space borne
515 measurements should be carried out continuously for upcoming new era of geostationary environmental satellite.

516 **4 Conclusions**

517 For the first time, we have retrieved NO₂ VCD data using airborne GeoTASO observations over the Seoul metropolitan
518 region—one of the most populous cities worldwide, the Busan metropolitan region—the second-largest city in South Korea,
519 and Anmyeon, with thermal power plants and industrial complexes. By retrieving NO₂ data using GeoTASO L1B radiance, it
520 was possible to observe the spatial distribution of NO₂ over these metropolitan and industrial regions. In the morning,
521 tropospheric NO₂ VCD over Seoul showed a strong horizontal gradient between rural and urban areas. In urban areas,
522 tropospheric NO₂ VCD was high, with values exceeding 3×10^{16} molecules cm⁻²; in rural areas, values were typically below
523 1×10^{16} molecules cm⁻². Extremely high values over 10×10^{16} molecules cm⁻² were also observed in both rural and urban
524 areas. In Anmyeon, GeoTASO observations showed NO₂ is mainly emitted from the chimneys of industrial complexes and
525 thermal power plants, and subsequently transported by wind approximately 30 km to the Yellow Sea of the west coast of the
526 Korean Peninsula. In the Busan metropolitan region, in the morning, tropospheric NO₂ VCDs showed a similar pattern to the
527 Seoul metropolitan region, with high values above the inter-city road. However, in contrast to Seoul, tropospheric NO₂ VCDs
528 in Busan decreased in the afternoon due to different weather conditions locally.

529 To compare the data retrieved from the GeoTASO system, we compared NO_{2,G} with NO_{2,O} obtained from the OMI, NO_{2,A}
530 obtained from Air-Korea, and NO_{2,P} obtained from the Pandora observation system. When the distance between two
531 observations was below 20 km or 0.05 degree within 30 min, the correlation coefficients were relatively high (R = 0.48, and
532 91, respectively). However, the correlation between NO_{2,G} and NO_{2,A} over the Seoul metropolitan region was very weak (R =
533 0.07) in the morning because of the more pronounced NO₂ horizontal gradient.

534 The GeoTASO system successfully observed NO₂ VCDs with a high horizontal spatial resolution for both metropolitan and
535 industrial regions. This demonstrates that airborne remote sensing measurements from GeoTASO, similar to GCAS, APEX
536 and others, can be a very effective tool for the validation of trace gases retrieved from environmental satellites, including the
537 OMI, TROPOMI, and GOME-2; these systems can obtain high-resolution measurements over relatively wide areas. However,
538 to validate geostationary environmental satellites with higher spatiotemporal resolutions, such as the GEMS, TEMPO, and
539 sentinel-4, additional validation strategies are needed. Based on error estimation, it can be concluded that aerosol properties
540 are relevant and should be determined and NO₂ vertical profile retrieval performed using, for example, LIDAR, MAX-DOAS,
541 and sondes. This is important because the accuracy of aerosol properties and the NO₂ vertical profiles affects the accuracy of
542 AMF calculations (Leitão et al., 2010; Hong et al., 2017; Lorente et al., 2017; Boersma et al., 2018). Furthermore, as we
543 observed in the Seoul metropolitan area, more closely spaced observations using ground-based remote sensing systems and in
544 situ measurements are needed as NO₂ displays large horizontal gradients, especially in the morning.

545 **Author contributions**

546 **GH** and **HH** designed and implemented the research. **KL** provided the CTM data. **GH** developed the code for model running
547 and performed the RTM simulations. **HH** and **UJ** contributed to the analysis of ground-based data. **GH** and **WC** carried out
548 the sensitivity test. **GH**, **KL**, **HH**, **UJ**, **WC**, and **JJS** revised and edited the paper. **HH**, **UJ**, and **WC** provided constructive
549 comments. All authors contributed to this works.

550 **Competing interests**

551 The authors declare that they have no conflict of interest.

552 **Acknowledgements**

553 Pandora data were obtained from the KORUS-AQ home pages of NASA's Goddard Space Flight Center
554 (<https://avdc.gsfc.nasa.gov/pub/DSCOVER/Pandora/DATA/KORUS-AQ/>). Ground-based NO₂ MR data were obtained
555 from Air-Korea (http://www.airkorea.or.kr/web/detailViewDown?pMENU_NO=125/). The authors would like to
556 thank KORUS-AQ campaign team for providing the GeoTASO and Pandora data.

557 **Funding**

558 This work was funded by the National Institute of Environmental Research (NIER) of Ministry of Environment [No. NIER-
559 2021-01-01-100].

560 **References**

- 561 Boersma, K. F., Eskes, H. J., and Brinksma, E. J.: Error analysis for tropospheric NO₂ retrieval from space: ERROR
562 ANALYSIS FOR TROPOSPHERIC NO₂, *J. Geophys. Res.*, 109, n/a-n/a, <https://doi.org/10.1029/2003JD003962>, 2004.
- 563 Boersma, K. F., Eskes, H. J., Richter, A., De Smedt, I., Lorente, A., Beirle, S., van Geffen, J. H. G. M., Zara, M., Peters, E.,
564 Van Roozendaal, M., Wagner, T., Maasakkers, J. D., van der A, R. J., Nightingale, J., De Rudder, A., Irie, H., Pinardi, G.,
565 Lambert, J.-C., and Compernelle, S. C.: Improving algorithms and uncertainty estimates for satellite NO₂ retrievals: results
566 from the quality assurance for the essential climate variables (QA4ECV) project, *Atmos. Meas. Tech.*, 11, 6651–6678,
567 <https://doi.org/10.5194/amt-11-6651-2018>, 2018.
- 568 Brauer, M., Hoek, G., Van Vliet, P., Meliefste, K., Fischer, P. H., Wijga, A., Koopman, L. P., Neijens, H. J., Gerritsen, J.,
569 Kerkhof, M., Heinrich, J., Bellander, T., and Brunekreef, B.: Air Pollution from Traffic and the Development of Respiratory
570 Infections and Asthmatic and Allergic Symptoms in Children, *Am J Respir Crit Care Med*, 166, 1092–1098,
571 <https://doi.org/10.1164/rccm.200108-007OC>, 2002.
- 572 Burrows, J. P., Hölzle, E., Goede, A. P. H., Visser, H., and Fricke, W.: SCIAMACHY—scanning imaging absorption
573 spectrometer for atmospheric cartography, *Acta Astronautica*, 35, 445–451, [https://doi.org/10.1016/0094-5765\(94\)00278-T](https://doi.org/10.1016/0094-5765(94)00278-T),
574 1995.
- 575 Burrows, J. P., Weber, M., Buchwitz, M., Rozanov, V., Ladstätter-Weissenmayer, A., Richter, A., DeBeek, R., Hoogen, R.,
576 Bramstedt, K., Eichmann, K.-U., Eisinger, M., and Perner, D.: The Global Ozone Monitoring Experiment (GOME): Mission
577 Concept and First Scientific Results, 56, 151–175, [https://doi.org/10.1175/1520-0469\(1999\)056<0151:TGOMEG>2.0.CO;2](https://doi.org/10.1175/1520-0469(1999)056<0151:TGOMEG>2.0.CO;2),
578 1999.
- 579 BYUN, D.: Science algorithms of the EPA Models-3 Community Multiscale Air Quality (CMAQ) Modeling System, 1999.
- 580 Byun, D. and Schere, K. L.: Review of the Governing Equations, Computational Algorithms, and Other Components of the
581 Models-3 Community Multiscale Air Quality (CMAQ) Modeling System, *Appl. Mech. Rev.*, 59, 51,
582 <https://doi.org/10.1115/1.2128636>, 2006.
- 583 Callies, J., Corpaccioli, E., Eisinger, M., Hahne, A., and Lefebvre, A.: GOME-2-Metop's second-generation sensor for
584 operational ozone monitoring, *ESA Bull*, 1, 28–36, 2000.
- 585 Castellanos, P., Boersma, K. F., Torres, O., and de Haan, J. F.: OMI tropospheric NO₂ air mass factors over South America:
586 effects of biomass burning aerosols, *Atmos. Meas. Tech.*, 8, 3831–3849, <https://doi.org/10.5194/amt-8-3831-2015>, 2015.

587 Chance, K. and Kurucz, R. L.: An improved high-resolution solar reference spectrum for earth's atmosphere measurements in
588 the ultraviolet, visible, and near infrared, *Journal of Quantitative Spectroscopy and Radiative Transfer*, 111, 1289–1295,
589 <https://doi.org/10.1016/j.jqsrt.2010.01.036>, 2010.

590 Chance, K. V. and Spurr, R. J. D.: Ring effect studies: Rayleigh scattering, including molecular parameters for rotational
591 Raman scattering, and the Fraunhofer spectrum, *Appl. Opt.*, 36, 5224, <https://doi.org/10.1364/AO.36.005224>, 1997.

592 Choi, S., Lamsal, L. N., Follette-Cook, M., Joiner, J., Krotkov, N. A., Swartz, W. H., Pickering, K. E., Loughner, C. P., Appel,
593 W., Pfister, G., Saide, P. E., Cohen, R. C., Weinheimer, A. J., and Herman, J. R.: Assessment of NO₂ observations during
594 DISCOVER-AQ and KORUS-AQ field campaigns, *Atmos. Meas. Tech.*, 13, 2523–2546, [https://doi.org/10.5194/amt-13-](https://doi.org/10.5194/amt-13-2523-2020)
595 [2523-2020](https://doi.org/10.5194/amt-13-2523-2020), 2020.

596 Choi, W. J.: Introducing the geostationary environment monitoring spectrometer, *J. Appl. Rem. Sens.*, 12, 1,
597 <https://doi.org/10.1117/1.JRS.12.044005>, 2018.

598 Choi, M., Lim, H., Kim, J., Lee, S., Eck, T. F., Holben, B. N., Garay, M. J., Hyer, E. J., Saide, P. E., and Liu, H.: Validation,
599 comparison, and integration of GOCI, AHI, MODIS, MISR, and VIIRS aerosol optical depth over East Asia during the 2016
600 KORUS-AQ campaign, *Atmospheric Measurement Techniques*, 12(8), 4619–4641, <https://doi.org/10.5194/amt-12-4619-2019>,
601 2019.

602 Chong, H., Lee, S., Kim, J., Jeong, U., Li, C., Krotkov, N. A., Nowlan, C. R., Al-Saadi, J. A., Janz, S. J., Kowalewski, M. G.,
603 Ahn, M.-H., Kang, M., Joiner, J., Haffner, D. P., Hu, L., Castellanos, P., Huey, L. G., Choi, M., Song, C. H., Han, K. M., and
604 Koo, J.-H.: High-resolution mapping of SO₂ using airborne observations from the GeoTASO instrument during the KORUS-
605 AQ field study: PCA-based vertical column retrievals, *Remote Sensing of Environment*, 241, 111725,
606 <https://doi.org/10.1016/j.rse.2020.111725>, 2020.

607 Choo, G.-H., Seo, J., Yoon, J., Kim, D.-R., and Lee, D.-W.: Analysis of long-term (2005–2018) trends in tropospheric NO₂
608 percentiles over Northeast Asia, *Atmospheric Pollution Research*, 11, 1429–1440, <https://doi.org/10.1016/j.apr.2020.05.012>,
609 2020.

610 Danckaert, T., Fayt, C., Van Roozendaal, M., De Smedt, I., Letocart, V., Merlaud, A., and Pinardi, G.: QDOAS Software user
611 manual, Belgian Institute for Space Aeronomy, 2016.

612 de Foy, B., Lu, Z., and Streets, D. G.: Satellite NO₂ retrievals suggest China has exceeded its NO_x reduction goals from the
613 twelfth Five-Year Plan, *Sci Rep*, 6, 35912, <https://doi.org/10.1038/srep35912>, 2016.

614 General, S., Pöhler, D., Sihler, H., Bobrowski, N., Frieß, U., Zielcke, J., Horbanski, M., Shepson, P. B., Stirm, B. H., Simpson,
615 W. R., Weber, K., Fischer, C., and Platt, U.: The Heidelberg Airborne Imaging DOAS Instrument (HAIDI) – a novel imaging
616 DOAS device for 2-D and 3-D imaging of trace gases and aerosols, *Atmos. Meas. Tech.*, 7, 3459–3485,
617 <https://doi.org/10.5194/amt-7-3459-2014>, 2014.

618 Guenther, A., Karl, T., Harley, P., Wiedinmyer, C., Palmer, P. I., and Geron, C.: Estimates of global terrestrial isoprene
619 emissions using MEGAN (Model of Emissions of Gases and Aerosols from Nature), *Atmos. Chem. Phys.*, 6, 3181–3210,
620 <https://doi.org/10.5194/acp-6-3181-2006>, 2006.

621 Guenther, A. B., Jiang, X., Heald, C. L., Sakulyanontvittaya, T., Duhl, T., Emmons, L. K., and Wang, X.: The Model of
622 Emissions of Gases and Aerosols from Nature version 2.1 (MEGAN2.1): an extended and updated framework for modeling
623 biogenic emissions, *Geosci. Model Dev.*, 5, 1471–1492, <https://doi.org/10.5194/gmd-5-1471-2012>, 2012.

624 Herman, J., Cede, A., Spinei, E., Mount, G., Tzortziou, M., and Abuhassan, N.: NO₂ column amounts from ground-based
625 Pandora and MFDOAS spectrometers using the direct-sun DOAS technique: Intercomparisons and application to OMI
626 validation, *J. Geophys. Res.*, 114, D13307, <https://doi.org/10.1029/2009JD011848>, 2009.

627 Herman, J., Spinei, E., Fried, A., Kim, J., Kim, J., Kim, W., Cede, A., Abuhassan, N., and Segal-Rozenhaimer, M.: NO₂ and
628 HCHO measurements in Korea from 2012 to 2016 from Pandora spectrometer instruments compared with OMI retrievals and

629 with aircraft measurements during the KORUS-AQ campaign, *Atmos. Meas. Tech.*, 11, 4583–4603,
630 <https://doi.org/10.5194/amt-11-4583-2018>, 2018.

631 Hong, H., Lee, H., Kim, J., Jeong, U., Ryu, J., and Lee, D.: Investigation of Simultaneous Effects of Aerosol Properties and
632 Aerosol Peak Height on the Air Mass Factors for Space-Borne NO₂ Retrievals, *Remote Sensing*, 9, 208,
633 <https://doi.org/10.3390/rs9030208>, 2017.

634 Jeong, U., and H. Hong: Assessment of tropospheric concentrations of NO₂ from the TROPOMI/Sentinel-5 Precursor for the
635 estimation of long-term exposure to surface NO₂ over South Korea, *Remote Sensing*, 13, 1877,
636 <https://doi.org/10.3390/rs13101877>, 2021a.

637 Jeong, U., and H. Hong: Comparison of total column and surface mixing ratio of carbon monoxide derived from the
638 TROPOMI/Sentinel-5 Precursor with In-Situ measurements from extensive ground-based network over South Korea, *Remote*
639 *Sensing*, 13, 3987, <https://doi.org/10.3390/rs13193987>, 2021b.

640 Judd, L. M., Al-Saadi, J. A., Valin, L. C., Pierce, R. B., Yang, K., Janz, S. J., Kowalewski, M. G., Szykman, J. J., Tiefengraber,
641 M., and Mueller, M.: The Dawn of Geostationary Air Quality Monitoring: Case Studies From Seoul and Los Angeles, *Front.*
642 *Environ. Sci.*, 6, 85, <https://doi.org/10.3389/fenvs.2018.00085>, 2018.

643 Judd, L. M., Al-Saadi, J. A., Janz, S. J., Kowalewski, M. G., Pierce, R. B., Szykman, J. J., Valin, L. C., Swap, R., Cede, A.,
644 Mueller, M., Tiefengraber, M., Abuhassan, N., and Williams, D.: Evaluating the impact of spatial resolution on tropospheric
645 NO₂ column comparisons within urban areas using high-resolution airborne data, *Atmos. Meas. Tech.*, 12, 6091–6111,
646 <https://doi.org/10.5194/amt-12-6091-2019>, 2019.

647 Judd, L. M., Al-Saadi, J. A., Szykman, J. J., Valin, L. C., Janz, S. J., Kowalewski, M. G., Eskes, H. J., Veefkind, J. P., Cede,
648 A., Mueller, M., Gebetsberger, M., Swap, R., Pierce, R. B., Nowlan, C. R., Abad, G. G., Nehrir, A., and Williams, D.:
649 Evaluating Sentinel-5P TROPOMI tropospheric NO₂ column densities with airborne and Pandora spectrometers near New
650 York City and Long Island Sound, *Atmos. Meas. Tech.*, 13, 6113–6140, <https://doi.org/10.5194/amt-13-6113-2020>, 2020.

651 Kendrick, C. M., Koonce, P., and George, L. A.: Diurnal and seasonal variations of NO, NO₂ and PM_{2.5} mass as a function of
652 traffic volumes alongside an urban arterial, *Atmospheric Environment*, 122, 133–141,
653 <https://doi.org/10.1016/j.atmosenv.2015.09.019>, 2015.

654 Kim, D., Lee, H., Hong, H., Choi, W., Lee, Y., and Park, J.: Estimation of Surface NO₂ Volume Mixing Ratio in Four
655 Metropolitan Cities in Korea Using Multiple Regression Models with OMI and AIRS Data, *Remote Sensing*, 9, 627,
656 <https://doi.org/10.3390/rs9060627>, 2017.

657 Kim, J., Jeong, U., Ahn, M.-H., Kim, J. H., Park, R. J., Lee, H., Song, C. H., Choi, Y.-S., Lee, K.-H., Yoo, J.-M., Jeong, M.-
658 J., Park, S. K., Lee, K.-M., Song, C.-K., Kim, S.-W., Kim, Y. J., Kim, S.-W., Kim, M., Go, S., Liu, X., Chance, K., Chan
659 Miller, C., Al-Saadi, J., Veihelmann, B., Bhartia, P. K., Torres, O., Abad, G. G., Haffner, D. P., Ko, D. H., Lee, S. H., Woo,
660 J.-H., Chong, H., Park, S. S., Nicks, D., Choi, W. J., Moon, K.-J., Cho, A., Yoon, J., Kim, S., Hong, H., Lee, K., Lee, H., Lee,
661 S., Choi, M., Veefkind, P., Levelt, P. F., Edwards, D. P., Kang, M., Eo, M., Bak, J., Baek, K., Kwon, H.-A., Yang, J., Park, J.,
662 Han, K. M., Kim, B.-R., Shin, H.-W., Choi, H., Lee, E., Chong, J., Cha, Y., Koo, J.-H., Irie, H., Hayashida, S., Kasai, Y.,
663 Kanaya, Y., Liu, C., Lin, J., Crawford, J. H., Carmichael, G. R., Newchurch, M. J., Lefer, B. L., Herman, J. R., Swap, R. J.,
664 Lau, A. K. H., Kurosu, T. P., Jaross, G., Ahlers, B., Dobber, M., McElroy, C. T., and Choi, Y.: New Era of Air Quality
665 Monitoring from Space: Geostationary Environment Monitoring Spectrometer (GEMS), 101, E1–E22,
666 <https://doi.org/10.1175/BAMS-D-18-0013.1>, 2020.

667 Kley, D. and McFarland, M.: Chemiluminescence detector for NO and NO₂, *Atmos. Technol.*; (United States), 12, 1980.

668 Kowalewski, M. G. and Janz, S. J.: Remote sensing capabilities of the GEO-CAPE airborne simulator, *SPIE Optical*
669 *Engineering + Applications*, San Diego, California, United States, 92181I, <https://doi.org/10.1117/12.2062058>, 2014.

670 Kowalewski, M.G., Janz, S., Al-Saadi, J.A., Good, W., Ruppert, L., Cole, J.: GeoTASO instrument characterization and
671 level1b radiance product generation, In: Proceedings of the 1st KORUS-AQ Science Team Meeting, Jeju, South Korea, 27
672 February–3 March 2017, 13. 2017

673 Lamsal, L. N., Martin, R. V., Parrish, D. D., and Krotkov, N. A.: Scaling Relationship for NO₂ Pollution and Urban Population
674 Size: A Satellite Perspective, *Environ. Sci. Technol.*, 47, 7855–7861, <https://doi.org/10.1021/es400744g>, 2013.

675 Lamsal, L. N., Janz, S. J., Krotkov, N. A., Pickering, K. E., Spurr, R. J. D., Kowalewski, M. G., Loughner, C. P., Crawford, J.
676 H., Swartz, W. H., and Herman, J. R.: High-resolution NO₂ observations from the Airborne Compact Atmospheric Mapper:
677 Retrieval and validation, *J. Geophys. Res. Atmos.*, 122, 1953–1970, <https://doi.org/10.1002/2016JD025483>, 2017.

678 Latza, U., Gerdes, S., and Baur, X.: Effects of nitrogen dioxide on human health: Systematic review of experimental and
679 epidemiological studies conducted between 2002 and 2006, *International Journal of Hygiene and Environmental Health*, 212,
680 271–287, <https://doi.org/10.1016/j.ijheh.2008.06.003>, 2009.

681 Lee, K., Yu, J., Lee, S., Park, M., Hong, H., Park, S. Y., Choi, M., Kim, J., Kim, Y., Woo, J.-H., Kim, S.-W., and Song, C. H.:
682 Development of Korean Air Quality Prediction System version 1 (KAQPS v1) with focuses on practical issues, *Geosci. Model*
683 *Dev.*, 13, 1055–1073, <https://doi.org/10.5194/gmd-13-1055-2020>, 2020.

684 Leitão, J., Richter, A., Vrekoussis, M., Kokhanovsky, A., Zhang, Q. J., Beekmann, M., and Burrows, J. P.: On the improvement
685 of NO₂ satellite retrievals–aerosol impact on the air mass factors, *Atmos. Meas. Tech.*, 3, 475–493, [https://doi.org/10.5194/amt-](https://doi.org/10.5194/amt-3-475-2010)
686 [3-475-2010](https://doi.org/10.5194/amt-3-475-2010), 2010.

687 Leitch, J. W., Delker, T., Good, W., Ruppert, L., Murcray, F., Chance, K., Liu, X., Nowlan, C., Janz, S. J., Krotkov, N. A.,
688 Pickering, K. E., Kowalewski, M., and Wang, J.: The GeoTASO airborne spectrometer project, SPIE Optical Engineering +
689 Applications, San Diego, California, United States, 92181H, <https://doi.org/10.1117/12.2063763>, 2014.

690 Levelt, P. F., van den Oord, G. H. J., Dobber, M. R., Malkki, A., Huib Visser, Johan de Vries, Stammes, P., Lundell, J. O. V.,
691 and Saari, H.: The ozone monitoring instrument, *IEEE Trans. Geosci. Remote Sensing*, 44, 1093–1101,
692 <https://doi.org/10.1109/TGRS.2006.872333>, 2006.

693 Lorente, A., Folkert Boersma, K., Yu, H., Dörner, S., Hilboll, A., Richter, A., Liu, M., Lamsal, L. N., Barkley, M., De Smedt,
694 I., Van Roozendaal, M., Wang, Y., Wagner, T., Beirle, S., Lin, J.-T., Krotkov, N., Stammes, P., Wang, P., Eskes, H. J., and
695 Krol, M.: Structural uncertainty in air mass factor calculation for NO₂ and HCHO satellite retrievals, *Atmos. Meas. Tech.*, 10,
696 759–782, <https://doi.org/10.5194/amt-10-759-2017>, 2017.

697 Ma, J. Z., Beirle, S., Jin, J. L., Shaiganfar, R., Yan, P., and Wagner, T.: Tropospheric NO₂ vertical column densities over
698 Beijing: results of the first three years of ground-based MAX-DOAS measurements (2008–2011) and satellite validation,
699 *Atmos. Chem. Phys.*, 13, 1547–1567, <https://doi.org/10.5194/acp-13-1547-2013>, 2013.

700 Malm, W. C. and Hand J. L.: An examination of the physical and optical properties of aerosols collected in the IMPROVE
701 program, *Atmospheric Environment*, 41, 3407– 3427, <https://doi.org/10.1016/j.atmosenv.2006.12.012>, 2007.

702 Merlaud, A., Constantin, D., Mingireanu, F., Mocanu, I., Maes, J., Fayt, C., Voiculescu, M., Murariu, G., Georgescu, L., Van
703 Roozendaal, M.: Small whiskbroom imager for atmospheric composition monitoring (SWING) from an unmanned aerial
704 vehicle (UAV), in: Proceedings of the 21st ESA Symposium on European Rocket & Balloon Programmes and related Research,
705 Thun, Switzerland pp.9–13, 2013.

706 Meier, A. C., Schönhardt, A., Bösch, T., Richter, A., Seyler, A., Ruhtz, T., Constantin, D.-E., Shaiganfar, R., Wagner, T.,
707 Merlaud, A., Van Roozendaal, M., Belegante, L., Nicolae, D., Georgescu, L., and Burrows, J. P.: High-resolution airborne
708 imaging DOAS measurements of NO₂ above Bucharest during AROMAT, *Atmos. Meas. Tech.*, 10, 1831–1857,
709 <https://doi.org/10.5194/amt-10-1831-2017>, 2017.

710 Merlaud, A., Tack, F., Constantin, D., Georgescu, L., Maes, J., Fayt, C., Mingireanu, F., Schuettmeyer, D., Meier, A. C.,
711 Schönardt, A., Ruhtz, T., Bellegante, L., Nicolae, D., Den Hoed, M., Allaart, M., and Van Roozendaal, M.: The Small

712 Whiskbroom Imager for atmospheric composition monitoring (SWING) and its operations from an unmanned aerial vehicle
713 (UAV) during the AROMAT campaign, *Atmos. Meas. Tech.*, 11, 551–567, <https://doi.org/10.5194/amt-11-551-2018>, 2018.

714 Nowlan, C. R., Liu, X., Leitch, J. W., Chance, K., González Abad, G., Liu, C., Zoogman, P., Cole, J., Delker, T., Good, W.,
715 Murcray, F., Ruppert, L., Soo, D., Follette-Cook, M. B., Janz, S. J., Kowalewski, M. G., Loughner, C. P., Pickering, K. E.,
716 Herman, J. R., Beaver, M. R., Long, R. W., Szykman, J. J., Judd, L. M., Kelley, P., Luke, W. T., Ren, X., and Al-Saadi, J. A.:
717 Nitrogen dioxide observations from the Geostationary Trace gas and Aerosol Sensor Optimization (GeoTASO) airborne
718 instrument: Retrieval algorithm and measurements during DISCOVER-AQ Texas 2013, *Atmos. Meas. Tech.*, 9, 2647–2668,
719 <https://doi.org/10.5194/amt-9-2647-2016>, 2016.

720 National Institute of Environmental Research (NIER) and National Aeronautics and Space Administration (NASA): KORUS-
721 AQ Final Science Synthesis Report, available at <https://espo.nasa.gov/sites/default/files/documents/5858211.pdf>, last access:
722 27 June 2022, 2020.

723 Nowlan, C. R., Liu, X., Leitch, J. W., Chance, K., A., González Abad, G., Liu, C., Zoogman, P., Cole, J., Delker, T., Good, W.,
724 Murcray, F., Ruppert, L., Soo, D., Follette-Cook, M. B., Janz, S. J., Kowalewski, M. G., Loughner, C. P., Pickering, K. E.,
725 Herman, J. R., Beaver, M. R., Long, R. W., Szykman, J. J., Judd, L. M., Kelley, P., Luke, W. T., Ren, W., and Al-Saadi, J. A.:
726 Nitrogen dioxide observations from the Geostationary Trace gas and Aerosol Sensor Optimization (GeoTASO) airborne
727 instrument: Retrieval algorithm and measurements during DISCOVER-AQ Texas 2013, *Atmos. Meas. Tech.*, 9, 2647–2668,
728 <http://doi.org/10.5194/atm-9-2647-2016>, 2016.

729 Nowlan, C. R., Liu, X., Janz, S. J., Kowalewski, M. G., Chance, K., Follette-Cook, M. B., Fried, A., González Abad, G.,
730 Herman, J. R., Judd, L. M., Kwon, H.-A., Loughner, C. P., Pickering, K. E., Richter, D., Spinei, E., Walega, J., Weibring, P.,
731 and Weinheimer, A. J.: Nitrogen dioxide and formaldehyde measurements from the GEOstationary Coastal and Air Pollution
732 Events (GEO-CAPE) Airborne Simulator over Houston, Texas, *Atmos. Meas. Tech.*, 11, 5941–5964,
733 <https://doi.org/10.5194/amt-11-5941-2018>, 2018.

734 Palmer, P. I., Jacob, D. J., Chance, K., Martin, R. V., Spurr, R. J. D., Kurosu, T. P., Bey, I., Yantosca, R., Fiore, A., and Li,
735 Q.: Air mass factor formulation for spectroscopic measurements from satellites: Application to formaldehyde retrievals from
736 the Global Ozone Monitoring Experiment, *J. Geophys. Res.*, 106, 14539–14550, <https://doi.org/10.1029/2000JD900772>, 2001.

737 Pastel, M., Pommereau, J.-P., Goutail, F., Richter, A., Pazmiño, A., Ionov, D., and Portafaix, T.: Construction of merged
738 satellite total O₃ and NO₂ time series in the tropics for trend studies and evaluation by comparison to NDACC SAOZ
739 measurements, *Atmos. Meas. Tech.*, 7, 3337–3354, <https://doi.org/10.5194/amt-7-3337-2014>, 2014.

740 Platt, U.: Differential absorption spectroscopy (DOAS), *Chem. Anal. Series*, 127, 27–83, 1994.

741 Platt, U., Stutz, J.: Differential absorption spectroscopy, in: *Differential Optical Absorption Spectroscopy*, Springer, Berlin,
742 Heidelberg, pp. 135–174, 2008.

743 Popp, C., Brunner, D., Damm, A., Van Roozendaal, M., Fayt, C., and Buchmann, B.: High-resolution NO₂ remote sensing
744 from the Airborne Prism EXperiment (APEX) imaging spectrometer, *Atmos. Meas. Tech.*, 5, 2211–2225,
745 <https://doi.org/10.5194/amt-5-2211-2012>, 2012.

746 Prasad, A. K., Singh, R. P., and Kafatos, M.: Influence of coal-based thermal power plants on the spatial–temporal variability
747 of tropospheric NO₂ column over India, *Environ Monit Assess*, 184, 1891–1907, <https://doi.org/10.1007/s10661-011-2087-6>,
748 2012.

749 Qin, K., Rao, L., Xu, J., Bai, Y., Zou, J., Hao, N., Li, S., and Yu, C.: Estimating Ground Level NO₂ Concentrations over
750 Central-Eastern China Using a Satellite-Based Geographically and Temporally Weighted Regression Model, *Remote Sensing*,
751 9, 950, <https://doi.org/10.3390/rs9090950>, 2017.

752 Richter, A., Burrows, J. P., Nüß, H., Granier, C., and Niemeier, U.: Increase in tropospheric nitrogen dioxide over China
753 observed from space, *Nature*, 437, 129–132, <https://doi.org/10.1038/nature04092>, 2005.

754 Rothman, L. S., Gordon, I. E., Barber, R. J., Dothe, H., Gamache, R. R., Goldman, A., Perevalov, V. I., Tashkun, S. A.,
755 Tennyson, J. HITEMP, the high-temperature molecular spectroscopic database. *Journal of Quantitative Spectroscopy and*
756 *Radiative Transfer*, 111(15), 2139–2150, 2010.

757 Schönhardt, A., Altube, P., Gerilowski, K., Krautwurst, S., Hartmann, J., Meier, A. C., Richter, A., and Burrows, J. P.: A wide
758 field-of-view imaging DOAS instrument for two-dimensional trace gas mapping from aircraft, *Atmos. Meas. Tech.*, 8, 5113–
759 5131, <https://doi.org/10.5194/amt-8-5113-2015>, 2015.

760 Shah, V., Jacob, D. J., Li, K., Silvern, R. F., Zhai, S., Liu, M., Lin, J., and Zhang, Q.: Effect of changing NO_x lifetime on the
761 seasonality and long-term trends of satellite-observed tropospheric NO₂ columns over China, *Atmos. Chem. Phys.*, 20, 1483–
762 1495, <https://doi.org/10.5194/acp-20-1483-2020>, 2020.

763 Skamarock, W., Klemp, J., Dudhia, J., Gill, D., Barker, D., Wang, W., Huang, X.-Y., and Duda, M.: A Description of the
764 Advanced Research WRF Version 3, UCAR/NCAR, <https://doi.org/10.5065/D68S4MVH>, 2008.

765 Spinei, E., Whitehill, A., Fried, A., Tiefengraber, M., Knepp, T. N., Herndon, S., Herman, J. R., Müller, M., Abuhassan, N.,
766 Cede, A., Richter, D., Walega, J., Crawford, J., Szykman, J., Valin, L., Williams, D. J., Long, R., Swap, R. J., Lee, Y., Nowak,
767 N., and Poche, B.: The first evaluation of formaldehyde column observations by improved Pandora spectrometers during the
768 KORUS-AQ field study, *Atmos. Meas. Tech.*, 11, 4943–4961, <https://doi.org/10.5194/amt-11-4943-2018>, 2018.

769 Spurr, R. and Christi, M.: On the generation of atmospheric property Jacobians from the (V)LIDORT linearized radiative
770 transfer models, *Journal of Quantitative Spectroscopy and Radiative Transfer*, 142, 109–115,
771 <https://doi.org/10.1016/j.jqsrt.2014.03.011>, 2014.

772 Tack, F., Merlaud, A., Iordache, M.-D., Danckaert, T., Yu, H., Fayt, C., Meuleman, K., Deutsch, F., Fierens, F., and Van
773 Roozendael, M.: High-resolution mapping of the NO₂ spatial distribution over Belgian urban areas based on airborne APEX
774 remote sensing, *Atmos. Meas. Tech.*, 10, 1665–1688, <https://doi.org/10.5194/amt-10-1665-2017>, 2017.

775 Tack, F., Merlaud, A., Meier, A. C., Vlemmix, T., Ruhtz, T., Iordache, M.-D., Ge, X., van der Wal, L., Schuettmeyer, D.,
776 Ardelean, M., Calcan, A., Constantin, D., Schönhardt, A., Meuleman, K., Richter, A., and Van Roozendael, M.:
777 Intercomparison of four airborne imaging DOAS systems for tropospheric NO₂ mapping—the AROMAPEX campaign, *Atmos.*
778 *Meas. Tech.*, 12, 211–236, <https://doi.org/10.5194/amt-12-211-2019>, 2019.

779 Tack, F., Merlaud, A., Iordache, M.-D., Pinardi, G., Dimitropoulou, E., Eskes, H., Bomans, B., Veeffkind, P., and Van
780 Roozendael, M.: Assessment of the TROPOMI tropospheric NO₂ product based on airborne APEX observations, *Atmos. Meas.*
781 *Tech.*, 14, 615–646, <https://doi.org/10.5194/amt-14-615-2021>, 2021.

782 Tzortziou, M., Parker, O., Lamb, B., Herman, J., Lamsal, L., Stauffer, R., and Abuhassan, N.: Atmospheric Trace Gas (NO₂
783 and O₃) Variability in South Korean Coastal Waters, and Implications for Remote Sensing of Coastal Ocean Color Dynamics,
784 *Remote Sensing*, 10, 1587, <https://doi.org/10.3390/rs10101587>, 2018.

785 Valks, P., Pinardi, G., Richter, A., Lambert, J.-C., Hao, N., Loyola, D., Van Roozendael, M., and Emmadi, S.: Operational
786 total and tropospheric NO₂ column retrieval for GOME-2, *Atmos. Meas. Tech.*, 4, 1491–1514, [https://doi.org/10.5194/amt-4-](https://doi.org/10.5194/amt-4-1491-2011)
787 1491-2011, 2011.

788 Vandaele, A. C., Hermans, C., Simon, P. C., Carleer, M., Colin, R., Fally, S., Mérienne, M. F., Jenouvrier, A., and Coquart,
789 B.: Measurements of the NO₂ absorption cross-section from 42 000 cm⁻¹ to 10 000 cm⁻¹ (238–1000 nm) at 220 K and 294 K,
790 *Journal of Quantitative Spectroscopy and Radiative Transfer*, 59, 171–184, [https://doi.org/10.1016/S0022-4073\(97\)00168-4](https://doi.org/10.1016/S0022-4073(97)00168-4),
791 1998.

792 Veeffkind, J. P., Aben, I., McMullan, K., Förster, H., de Vries, J., Otter, G., Claas, J., Eskes, H. J., de Haan, J. F., Kleipool, Q.,
793 van Weele, M., Hasekamp, O., Hoogeveen, R., Landgraf, J., Snel, R., Tol, P., Ingmann, P., Voors, R., Kruizinga, B., Vink, R.,
794 Visser, H., and Levelt, P. F.: TROPOMI on the ESA Sentinel-5 Precursor: A GMES mission for global observations of the
795 atmospheric composition for climate, air quality and ozone layer applications, *Remote Sensing of Environment*, 120, 70–83,
796 <https://doi.org/10.1016/j.rse.2011.09.027>, 2012.

797 Vlemmix, T., Ge, X., de Goeij, B. T. G., van der Wal, L. F., Otter, G. C. J., Stammes, P., Wang, P., Merlaud, A., Schüttemeyer,
798 D., Meier, A. C., Veeffkind, J. P., and Levelt, P. F.: Retrieval of tropospheric NO₂ columns over Berlin from high-resolution
799 airborne observations with the spectrolite breadboard instrument, *Atmos. Meas. Tech. Discuss.*, [https://doi.org/10.5194/amt-](https://doi.org/10.5194/amt-2017-257)
800 [2017-257](https://doi.org/10.5194/amt-2017-257), in review, 2017.

801 Wiedinmyer, C., Quayle, B., Geron, C., Belote, A., McKenzie, D., Zhang, X., O'Neill, S., and Wynne, K. K.: Estimating
802 emissions from fires in North America for air quality modeling, *Atmospheric Environment*, 40, 3419–3432,
803 <https://doi.org/10.1016/j.atmosenv.2006.02.010>, 2006.

804 Wiedinmyer, C., Akagi, S. K., Yokelson, R. J., Emmons, L. K., Al-Saadi, J. A., Orlando, J. J., and Soja, A. J.: The Fire
805 INventory from NCAR (FINN): a high resolution global model to estimate the emissions from open burning, *Geosci. Model*
806 *Dev.*, 4, 625–641, <https://doi.org/10.5194/gmd-4-625-2011>, 2011.

807 Wold, S., Esbensen, K., and Geladi, P.: Principal component analysis, *Chemometrics and Intelligent Laboratory Systems*, 2,
808 37–52, [https://doi.org/10.1016/0169-7439\(87\)80084-9](https://doi.org/10.1016/0169-7439(87)80084-9), 1987.

809 Woo, J.-H., Choi, K.-C., Kim, H. K., Baek, B. H., Jang, M., Eum, J.-H., Song, C. H., Ma, Y.-I., Sunwoo, Y., Chang, L.-S., and
810 Yoo, S. H.: Development of an anthropogenic emissions processing system for Asia using SMOKE, *Atmospheric Environment*,
811 58, 5–13, <https://doi.org/10.1016/j.atmosenv.2011.10.042>, 2012.

812 Zoogman, P., Liu, X., Suleiman, R. M., Pennington, W. F., Flittner, D. E., Al-Saadi, J. A., Hilton, B. B., Nicks, D. K.,
813 Newchurch, M. J., Carr, J. L., Janz, S. J., Andraschko, M. R., Arola, A., Baker, B. D., Canova, B. P., Chan Miller, C., Cohen,
814 R. C., Davis, J. E., Dussault, M. E., Edwards, D. P., Fishman, J., Ghulam, A., González Abad, G., Grutter, M., Herman, J. R.,
815 Houck, J., Jacob, D. J., Joiner, J., Kerridge, B. J., Kim, J., Krotkov, N. A., Lamsal, L., Li, C., Lindfors, A., Martin, R. V.,
816 McElroy, C. T., McLinden, C., Natraj, V., Neil, D. O., Nowlan, C. R., O'Sullivan, E. J., Palmer, P. I., Pierce, R. B., Pippin, M.
817 R., Saiz-Lopez, A., Spurr, R. J. D., Szykman, J. J., Torres, O., Veeffkind, J. P., Veihelmann, B., Wang, H., Wang, J., and
818 Chance, K.: Tropospheric emissions: Monitoring of pollution (TEMPO), *Journal of Quantitative Spectroscopy and Radiative*
819 *Transfer*, 186, 17–39, <https://doi.org/10.1016/j.jqsrt.2016.05.008>, 2017.

820